

# Numerical simulation of interfacial flows by smoothed particle hydrodynamics <sup>☆</sup>

Andrea Colagrossi <sup>\*</sup>, Maurizio Landrini

*INSEAN, The Italian Ship Model Basin, Via di Vallerano 139, 00128 Rome, Italy*

Received 29 January 2003; received in revised form 11 June 2003; accepted 17 June 2003

---

## Abstract

An implementation of the smoothed particle hydrodynamics (SPH) method is presented to treat two-dimensional interfacial flows, that is, flow fields with different fluids separated by sharp interfaces. Test cases are presented to show that the present formulation remains stable for low density ratios. In particular, results are compared with those obtained by other solution techniques, showing a good agreement. The classical dam-break problem is studied by the present two-phase approach and the effects of density-ratio variations are discussed. The role of air entrapment on loads is discussed.

© 2003 Elsevier B.V. All rights reserved.

**Keywords:** Interface flows; Multi-phase flows; Fluid–structure interactions; Impact flows; Air-cushion effect; Smoothed particle hydrodynamics

---

## 1. Introduction

In many circumstances, violent fluid–structure interactions lead to air entrapment and multi-phase flows. In marine and coastal engineering applications [11,31], the dynamics of the entrapped air at the impact may play a dominant role during the process and contribute to the high pressure maxima and pressure oscillations. Therefore, neglecting the air dynamics in impact flows may result in an incorrect approximation, particularly in predicting the short-time pressure characteristics (i.e., time-scales much shorter than the characteristic wave period) such as the pressure maxima, pressure rise times, and pressure oscillations.

A number of numerical techniques have been proposed to model flow fields with free surfaces or, more in general, with (sharp) interfaces separating immiscible fluids. Broad reviews are given in [34,35]. Most of the proposed and successful methods are based on the use of an Eulerian grid spanning the whole domain

---

<sup>☆</sup> This paper is dedicated to the memory of Maurizio Landrini who died only 40 years old in a tragic accident. Still very young he made significant scientific contributions to non-linear free-surface phenomena in hydrodynamics.

<sup>\*</sup> Corresponding author. Tel.: +39-06-50299343; fax: +39-06-5070619.

E-mail address: [a.colagrossi@insean.it](mailto:a.colagrossi@insean.it) (A. Colagrossi).

(possibly including different fluids) where the fluid-flow equations are solved and coupled with a suitable technique to capture or track the interface.

A more limited number of approaches is based on the Lagrangian tracking of fluid elements, either distributed near the interface or all over the fluid domain. Among the latter, smoothed particle hydrodynamics (SPH) is a fully Lagrangian mesh-less technique originally developed to deal with astro-dynamical problems [22] and successfully extended to a variety of fluid-dynamic systems [19,20]. Though it can be computationally more expensive than other Eulerian methods, SPH features a remarkable flexibility in handling complex flow fields and in including physical effects.

In particular, in a series of papers, Monaghan [21,25] has shown the SPH capability to treat free-surface flows with breaking and multi-phase flows with small density differences between the considered media [23,24]. When applying this approach to the air–water case, we found that severe instabilities develop along the fluid interface which prevented SPH to work.

In this paper, it is presented an original SPH implementation to handle two-dimensional interface flows with low density ratio. The key element of the present algorithm is a new form of the particle evolution equations, derived following [5], which improves the stability and removes fictitious surface-tension effects present in the standard SPH implementation [13]. Further improvements have been achieved by using: (i) a periodic re-initialization of the density field based on a moving-least-square interpolation [2] and (ii) a generalized form of Balsara's correction [3], to the usual SPH artificial viscosity. The last treatments are beneficial also for SPH computations of free-surface flows.

In the following, first the general concepts of the SPH modelling for incompressible interfacial flows are given, and the standard SPH implementation is described. The difficulty in modelling two-phase flows with small density ratios is then discussed for the case of a gas bubble rising through water. On this ground, the present SPH-implementation is introduced and described in details. The effect of the many adaptations is discussed by considering the rising-bubble problem and the dam-break problem. The latter is finally studied, with more emphasis on the physics of the violent impact of water against a fixed structure and the effect of entrapped air on the resulting loads.

## 2. SPH formulation for interfacial flows

### 2.1. Basic aspects of the SPH method for incompressible flows

In SPH methods, the fluid field is represented as a collection of  $N$  particles interacting with each other through evolution equations of the general form

$$\begin{aligned}\frac{d\rho_i}{dt} &= -\rho_i \sum_j \mathcal{M}_{ij}, \\ \frac{d\mathbf{u}_i}{dt} &= -\frac{1}{\rho_i} \sum_j \mathcal{F}_{ij} + \mathbf{f}_i, \\ \frac{d\mathbf{x}_i}{dt} &= \mathbf{u}_i.\end{aligned}\tag{1}$$

The interaction terms  $\mathcal{M}_{ij}, \mathcal{F}_{ij}$  follow from mass- and momentum-conservation equations and contain the density  $\rho_i$ , the velocity  $\mathbf{u}_i$  and the pressure  $p_i$  of the particles. The force  $\mathbf{f}_i$  can be any body force, though in the following only the action of the gravity will be considered. Finally, the last equation in (1) describes the motion of the  $i$ th particle. A rigorous derivation of SPH equations from the equation of fluid dynamics is given in [4], while [20] provides a more general presentation of the SPH method and its potential applications.

The interaction terms  $\mathcal{F}_{ij}$  model (at least) pressure interactions and contain the pressure  $p_i$ . In this paper, we mainly focus on the SPH-modelling of incompressible inviscid fluids and, following [21], the pressure particle is uniquely determined by the value of the density  $\rho_i$  through a state equation of the form

$$p(\rho) = P_0 \left[ \left( \frac{\rho}{\rho_0} \right)^\gamma - 1 \right] + \chi. \quad (2)$$

The constant background pressure  $\chi$  is added in two-phase flow simulations in confined domains, while  $\chi = 0$  is used for free-surface flows. The parameters  $P_0, \rho_0, \gamma$  are chosen to have maximum density oscillations of order of  $\mathcal{O}(1\%)$  around the reference value  $\rho_0$ . In practice, this is accomplished by choosing the sound speed  $c_s^2 = dp/d\rho$ , 10 times or more larger than the highest fluid velocity expected in the analyzed physical problem. As discussed later, the numerical stability of the method is related also to the local value of  $c_s$ . The use of the actual speed of sound in water would imply a time step too small for any practical use.

By assuming an explicit link between pressure and density, we do not need anymore to solve for the Poisson equation for the pressure. Therefore, the method does not require the solution of an algebraic problem and the memory occupation is just proportional to the number of particles. The particles can be arbitrarily scattered over the fluid domain leading to a completely grid-free method. The interaction terms can be computed independently of each other, resulting in an explicit algorithm which can be easily implemented on parallel computers.

The method is rather robust, even for large free-surface fragmentation and folding, efficient and relatively easy-to-code at least in its most naive implementation. Modelling of viscous, see e.g. [27], and of turbulent flows is less obvious. Finally, the stability analysis is still an open problem [26].

Alternative formulations of particle methods have been presented to model exactly incompressible fluids [10,14]. In particular, in [10], the authors have shown that the better stability properties of their incompressible formulation allow a larger time step and therefore the total CPU time is of the same order as in the weakly compressible approach. We have preferred the latter because of the higher resolution allowed for a given memory occupation.

It is worth to mention that the state equation (2) describes also the iso-entropic evolution of a gas, and system (1) suffices to describe the gas motion without solving explicitly the energy equation. Under this simplifying assumption, the model is still applicable when the fluid compressibility matters. As discussed later, this approximation can be accurate enough for studying air-cushion effects in impact phenomena.

## 2.2. Standard SPH formulation

The actual form of the interaction terms follows from the interpolation integral:

$$\langle u(\mathbf{x}) \rangle = \int_{\Omega} u(\mathbf{y}) W(\mathbf{x} - \mathbf{y}; h) dV_{\mathbf{y}}, \quad (3)$$

adopted to represent the fluid-flow variable in the domain  $\Omega$  and using a discrete form of it to derive approximations of the conservation equations. Eq. (3) can be interpreted as a reconstruction  $\langle u(\mathbf{x}) \rangle$  of the field  $u(\mathbf{y})$  in terms of the data sampled through the sampling function  $W(\mathbf{x} - \mathbf{y})$ . The parameter  $h$ , often called *smoothing length*, is a measure of the support of  $W$ , i.e., where  $W$  differs from zero. Physically,  $h$  is also representative of the domain of influence of  $\mathbf{y}$ . In the SPH framework,  $W(\mathbf{x} - \mathbf{y})$  is called *smoothing function* or *kernel*, and has the following properties:

- $W(\mathbf{x} - \mathbf{y}) \geq 0$  for  $\mathbf{x} \in \Omega_y \subset \Omega$ , and zero otherwise.
- $\int_{\Omega} W(\mathbf{x} - \mathbf{y}, h) dV_{\mathbf{y}} = 1$ .
- $W(\mathbf{x} - \mathbf{y}, h)$  decreases monotonously as  $|\mathbf{x} - \mathbf{y}|$  increases.

In the limit for  $h \rightarrow 0$ , the kernel function  $W$  becomes a Dirac delta function, and therefore

$$\lim_{h \rightarrow 0} \int_{\Omega} u(\mathbf{y}) W(\mathbf{x} - \mathbf{y}; h) dV_{\mathbf{y}} \equiv u(\mathbf{x}).$$

Formally, we can deduce approximations of any derivative of the field  $u$  by differentiating (3).

In practical computations, the smoothing function affects both the CPU requirements and the stability properties of the algorithm. In two dimensions, we have tested B-spline kernels of third and fifth order, as well as the Gaussian kernel

$$W(s, h) = \frac{1}{\pi h^2} e^{-(s/h)^2},$$

where  $s = |\mathbf{x} - \mathbf{y}|$ . In principle, this kernel does not have a compact support and in its use we introduced a cut-off limit  $\delta$  and renormalized  $W$  to match the property of unit integral

$$W(s, h, \delta) = \frac{e^{-(s/h)^2} - e^{-(\delta/h)^2}}{2\pi \int_0^{\delta} s (e^{-(s/h)^2} - e^{-(\delta/h)^2}) ds}. \quad (4)$$

In the practice, we usually choose  $\delta = 3h$  which is the same radius of the fifth-order B-spline support. After some tests, we adopted (4) because of the better stability properties [26] and the larger code efficiency.

In a widely used approach, the velocity field is approximated as

$$\langle \mathbf{u}_i \rangle \simeq \sum_j \mathbf{u}_j W_{ji} dV_j, \quad (5)$$

where  $W_{ji} = W(\mathbf{x}_i - \mathbf{x}_j; h)$ . Further, from now on we consider  $\langle \mathbf{u}_i \rangle \simeq \mathbf{u}_i$  and will not make distinction between the field and its SPH approximation. During its evolution, each particle carries a constant mass  $m_j$  and therefore  $dV_j = m_j/\rho_j$ . Locally conservative expressions for divergence and gradient operators are

$$\begin{aligned} \operatorname{div}(\mathbf{u}_i) &= \sum_j (\mathbf{u}_j - \mathbf{u}_i) \cdot \nabla W_{ji} \frac{m_j}{\rho_i}, \\ \nabla \mathcal{A}_i &= \sum_j (\mathcal{A}_j - \mathcal{A}_i) \nabla W_{ji} \frac{m_j}{\rho_i}. \end{aligned} \quad (6)$$

Here, the gradient operator  $\nabla$  is taken with respect to the variable  $\mathbf{x}_i$ . Finally, a commonly used form of the pressure gradient is

$$\nabla p_i = \rho_i \sum_j \left( \frac{p_j}{\rho_j^2} + \frac{p_i}{\rho_i^2} \right) \nabla W_{ij} m_j. \quad (7)$$

With these premises, in the following we assume:

$$\begin{aligned} \mathcal{M}_{ij} &= (\mathbf{u}_j - \mathbf{u}_i) \cdot \nabla W_{ji} \frac{m_j}{\rho_i}, \\ \mathcal{F}_{ij} &= \rho_i \left( \frac{p_j}{\rho_j^2} + \frac{p_i}{\rho_i^2} \right) \nabla W_{ij} m_j, \end{aligned} \quad (8)$$

as “standard” form of the interaction terms, though many variations have been proposed in the literature [20,21].

The above recalled implementation of the SPH method has been applied to the test case sketched in the left plot of Fig. 1: a circular bubble of fluid  $Y$  is free to rise through the initially quiescent heavier fluid  $X$ . Only the left side of the fluid domain is plotted because of the symmetry. The considered density

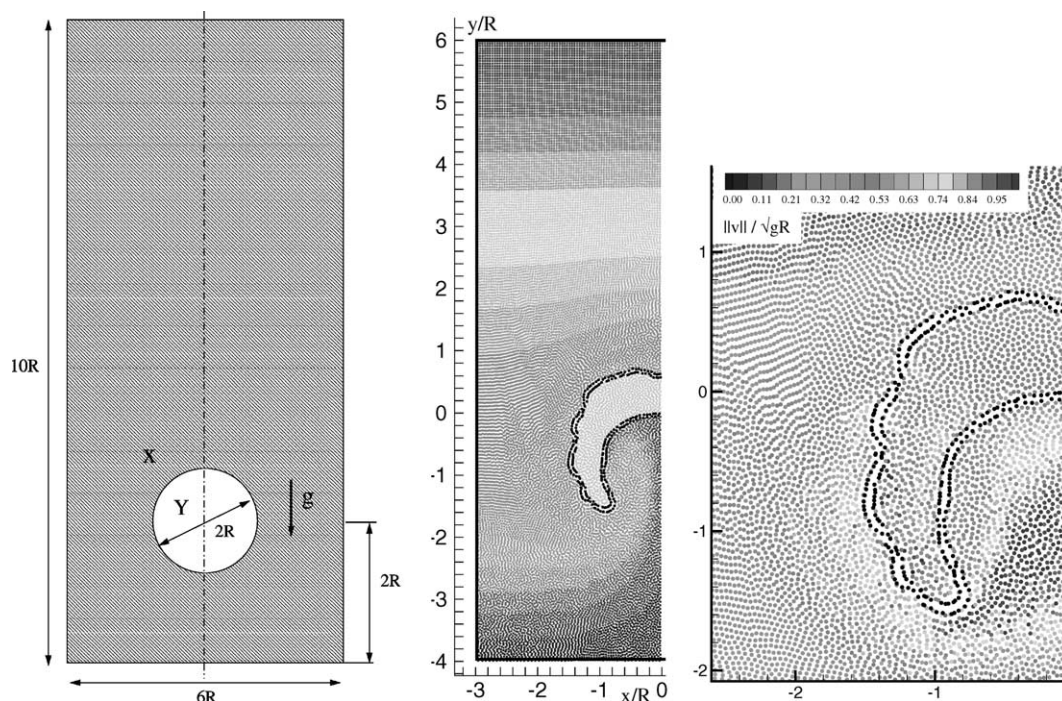


Fig. 1. Bubble of fluid  $Y$  rising through the heavier fluid  $X$ . Left: sketch of the problem and adopted nomenclature. Center: flow field for density ratio  $\rho_Y/\rho_X = 0.5$  and  $t(g/R)^{1/2} = 5.04$ . Right: enlarged view of the velocity field around the bubble interface.

ratio is  $\rho_Y/\rho_X = 0.5$ . The number of particles used in this simulation is  $N = 18,352$  ( $N_X = 17,394$ ,  $N_Y = 958$ ), with a smoothing length  $h/R = 5.4 \times 10^{-2}$ . The ratio of the smoothing length to the initially uniform particle spacing, say  $\Delta x$ , results to be about 1.33. This value for  $h/\Delta x$  is used in all the simulations presented in the following. As for instance reported in [17], to choose  $h/\Delta x$ , some authors suggest the practical rule that functions of the form  $ax + by + c$  have to be reproduced when particles are distributed on a Cartesian uniform lattice. With  $h/\Delta x = 1.33$  and the adopted kernel, this rule is satisfied with an error of order of  $10^{-4}$ . Clearly, this reproduction ability is no longer true as soon as the particles move. For the state equations, we have selected:  $p_{0,X}/\rho_X gR = 114$ ,  $\gamma_X = 7$ , therefore  $c_{s,X}/(gR)^{1/2} = 28.28$ ,  $p_{0,Y} = p_{0,X}$  and  $\gamma_Y = 7$ , resulting in  $c_{s,Y}/(gR)^{1/2} = 40$ . A fourth-order Runge–Kutta scheme with adaptive choice of the time step  $\delta t$  according to a stability criterium discussed later has been adopted for time stepping the solution. At the beginning of the simulation  $\delta t(g/R)^{1/2} = 3.4 \times 10^{-3}$ . As the bubble rises a jet is formed in its rear and approaches the highest point of the bubble. The jet slows down and broadens and the bubble attains a horseshoe form. The center plot shows the fluid-flow configuration for  $t(g/R)^{1/2} = 5.04$ . The heaviest particles are colored according to their initial vertical height to show the mixing of the fluid  $X$  induced by the bubble motion, while  $Y$ -fluid particles have a uniform color. An enlarged view is presented in the right plot of the same figure, where the color contour of the velocity magnitude is also shown.

Although the shown bubble interface appears somewhat irregular, the computation continued without any difficulty. The behavior changes for smaller density ratios, where the simulation stops almost immediately due to the development of a strong instability localized around the fluid interface. This is shown in Fig. 2, where the velocity field is presented for decreasing density ratios. The smaller  $\rho_Y/\rho_X$  is, the sooner the instability appears. The color contours give the pressure field which is almost everywhere still hydro-

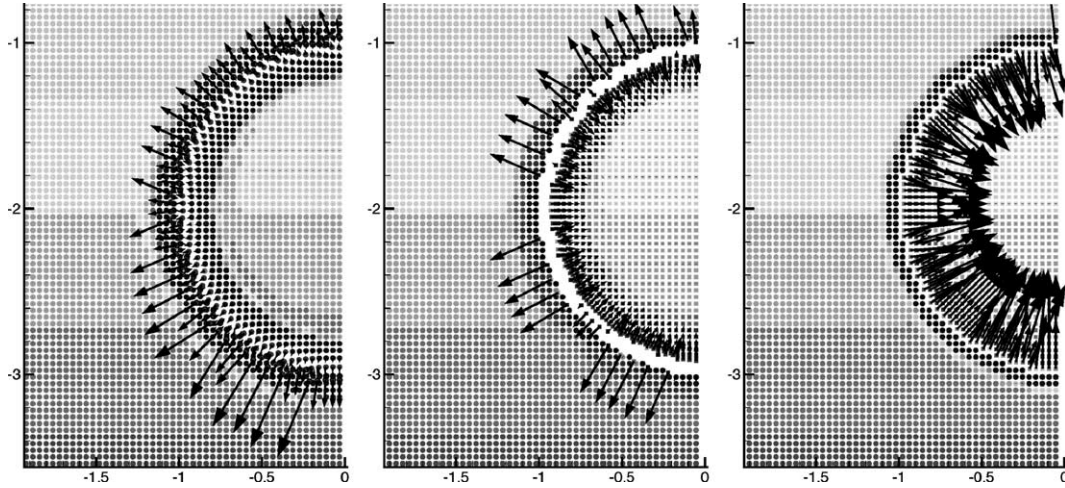


Fig. 2. Bubble of fluid  $Y$  rising through the heavier fluid  $X$ . Instability of the standard SPH method for  $\rho_Y/\rho_X = 0.1$  ( $(t(gR)^{1/2} = 1.51 \times 10^{-3})$ ,  $\rho_Y/\rho_X = 0.01$  ( $(t(gR)^{1/2} = 5.65 \times 10^{-4})$  and  $\rho_Y/\rho_X = 0.001$  ( $(t(gR)^{1/2} = 1.72 \times 10^{-5})$ , from left to right, respectively.

static, with large short-length oscillations around the interface. Here, the particles attain large velocities, in opposite directions on the two sides of the interface and the solution rapidly deteriorates.

By using the recalled standard SPH implementation for the considered test case, we never succeeded in dealing with density ratios  $\rho_Y/\rho_X \leq 0.1$ . In the next section, we present an SPH implementation to deal with interface flows with small density ratios (we tested down to the air–water density ratio, i.e.,  $\rho_Y/\rho_X = 0.001$ ). In our experience, the presented modifications to the standard SPH implementation improve the solution quality also for free-surface flows.

### 2.3. Present SPH formulation for interfacial flows

The derivation of Eq. (7) for the pressure gradient is based on the use of the identity

$$\frac{\nabla p}{\rho} = \nabla \left( \frac{p}{\rho} \right) + p \frac{\nabla \rho}{\rho^2}. \quad (9)$$

For free-surface flows, that is  $\rho_Y/\rho_X = 0$ , we can assume  $p \rightarrow 0$  as one approaches the free surface. Hence, the last term in (9) vanishes and smooths out the presence of the density gradient which is defined only in the fluid side. For interface flows, the pressure is continuous and generally different from zero while the density jumps sharply across the interface.

This circumstance is illustrated by considering the two-dimensional flow generated after the breaking of a dam, as sketched in Fig. 3. A vertical wall is placed at a given distance from the broken dam, and the fluid flowing along the initially dry-deck impacts eventually against it. After a run up–run down cycle, the water overturns backwards onto the underlying fluid. The simulations were performed by the new SPH implementation, and all the modifications discussed in the following paragraphs have been adopted. Figs. 4 and 5 show the flow field when the plunging-breaker hits the underlying water, forming a closed loop entrapping air (in the two-phase flow simulation). The right-side plots present enlarged details of the pressure field. The gross motion of the heaviest fluid is practically not affected by the presence of the air, as the comparison between the left-side plots shows. On the contrary, the large deformations of the water (first) and the air entrainment (then) result in an air–water pressure field which largely differs from the free-surface case. In the

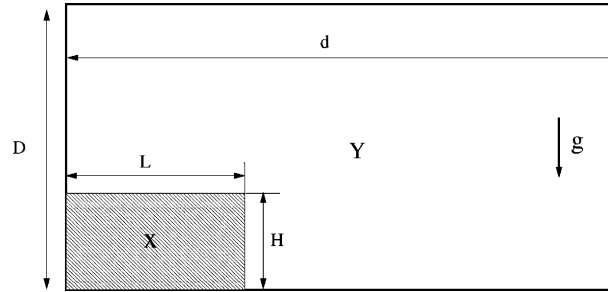


Fig. 3. Dam-break problem and impact against a vertical rigid wall. Left: sketch of the problem and adopted nomenclature. Right: main numerical parameters adopted for the simulations in Figs. 4 and 5. Geometric parameters  $L/H = 2$ ,  $D/H = 3$  and  $d/H = 5.366$ .  $N_X = 4900$ ,  $N_Y = 34,172$ ;  $P_{0,X}/(\rho_X g H) = 17.4$ ,  $P_{0,Y} = P_{0,X}$ ;  $\gamma_X = 7$ ,  $\gamma_Y = 1.4$ ;  $c_{s,X}/(gH)^{1/2} = 10.9$ ,  $c_{s,Y}/(gH)^{1/2} = 155$ ;  $h/H = 2.69 \times 10^{-2}$ ,  $\delta t(g/H)^{1/2} = 4.51 \times 10^{-4}$ .

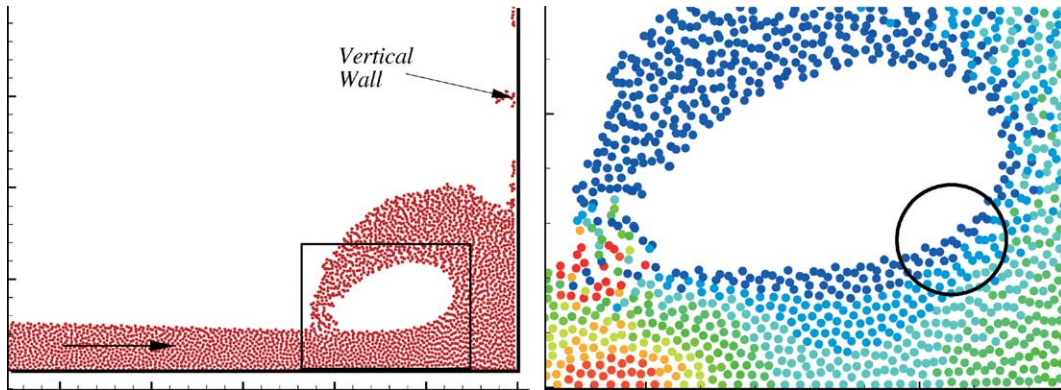


Fig. 4. Free-surface flow ( $\rho_Y/\rho_X = 0$ ) generated by the breaking of a dam (cf. Fig. 3). Fluid-flow configuration (left) and pressure field (right) after the impact of the water front against a vertical wall,  $t(g/H)^{1/2} = 6.1$ .

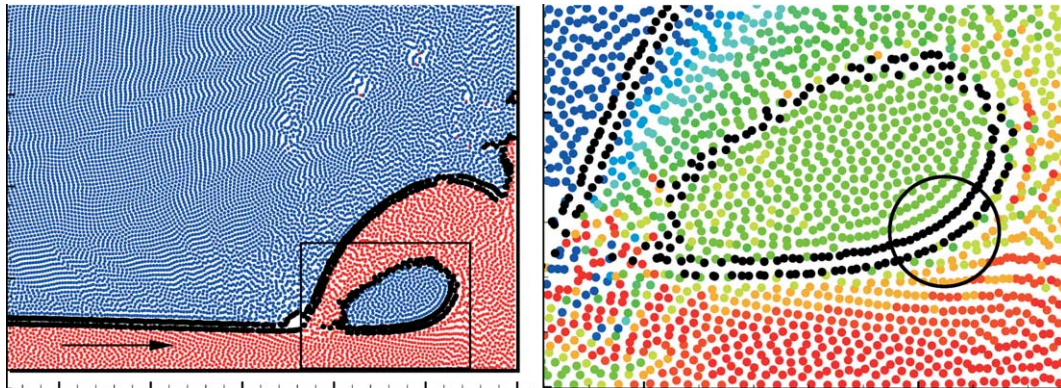


Fig. 5. Interface flow ( $\rho_Y/\rho_X = 0.001$ ) generated by the breaking of a dam (cf. Fig. 3). Interface configuration (left) and pressure field (right) after the impact of the water front against a vertical wall,  $t(g/H)^{1/2} = 6.1$ .



latter, right plot in Fig. 4, the pressure drops to zero when approaching the free surface. In the air–water flow, right plot in Fig. 5, it is visible the rise of the pressure due to the closure and compression of the entrapped air. Consistently, the pressure differs from zero at the interface, with a smooth transition between the two media. The density is discontinuous across the interface.

The presence of such a sharp density gradient at the interface is the main source of the severe numerical instability shown before, which prevented the standard SPH formulation to be applicable to flows with large density differences between the two media. To avoid this, we have used the discrete approximations

$$\begin{aligned}\operatorname{div}(\mathbf{u}_i) &= \sum_j (\mathbf{u}_j - \mathbf{u}_i) \cdot \nabla W_{ji} \frac{m_j}{\rho_j}, \\ \nabla \mathcal{A}_i &= \sum_j (\mathcal{A}_j - \mathcal{A}_i) \nabla W_{ji} \frac{m_j}{\rho_j}.\end{aligned}\quad (10)$$

The main difference between (10) and the typically adopted Eqs. (6) is the use of  $m_j/\rho_j$  instead of  $m_j/\rho_i$ , which becomes crucial for small density ratios. Finally, it can be shown that the pressure gradient in the form

$$\nabla p_i = \sum_j (p_j + p_i) \nabla W_{ji} dV_j \quad (11)$$

is variationally consistent with (10), see [5]. Eqs. (10) and (11) are still locally conservative. On this ground, in the present formulation the interaction terms take the form

$$\begin{aligned}\mathcal{M}_{ij} &= (\mathbf{u}_j - \mathbf{u}_i) \cdot \nabla W_{ji} \frac{m_j}{\rho_j}, \\ \mathcal{F}_{ij} &= (p_j + p_i) \nabla W_{ji} \frac{m_j}{\rho_j}.\end{aligned}\quad (12)$$

The improved capabilities of the present SPH implementation are shown in Fig. 6, where the problem of the rising bubble is shown for the air–water density ratio. The total number of particles is  $N = 18352$ , respectively,  $N_X = 17,394$  for the water phase and  $N_Y = 958$  for the air bubble. The smoothing length is  $h/R = 5.4 \times 10^{-2}$ . For the equation of state we have  $P_{0,X}/(\rho_X gR) = 114$ ,  $\gamma_X = 7$ ,  $c_{s,X}/(gR)^{1/2} = 28.28$  in water, and  $P_{0,X} = P_{0,Y}$ ,  $\gamma_Y = 1.4$ ,  $c_{s,Y}/(gR)^{1/2} = 400$  in air. The initial time stepping is  $\delta t(g/R)^{1/2} = 3.2 \times 10^{-4}$ .

In the same figure, the reference solution from Fig. 14, p. 156 in [37] is also plotted. This solution is obtained by solving the Navier–Stokes equations on a fixed grid spanning over the two media. The interface is captured by a Level-Set algorithm. The overall agreement during the whole evolution is quite satisfactory. As time passes, the upwelling water motion deforms the bubble which attains a horseshoe shape. The jet broadens, the tips of the bubble roll up and smaller bubbles are eventually detached. Before the pinch off, the largest difference observed is related to the thickness of the bubble along the line of symmetry, slightly smaller in the Level-Set computations. Later on, the Level-Set solution predicts the formation of three bubbles at each side: the largest one agrees with the present SPH results, while the smaller ones are not predicted by our method. Later on, in the Level-Set simulation those smaller bubbles disappear, probably because of numerical errors in mass conservation.

Fig. 7 and Table 1 report a convergence study based on  $N$ -,  $4N$ - and  $16N$ -particle simulations, respectively. The relative change

$$\varepsilon(f, n, m, \tau) = \int_0^\tau |f(t, m) - f(t, n)| dt \bigg/ \int_0^\tau |f(t, n)| dt$$

of the quantity  $f$  between simulations with ending time  $\tau$  and based on  $m$  and  $n$  particles is given for some local and global quantities. Namely, bubble thickness along  $x = 0$ , area of the bubble, center of mass  $Y_b$  of



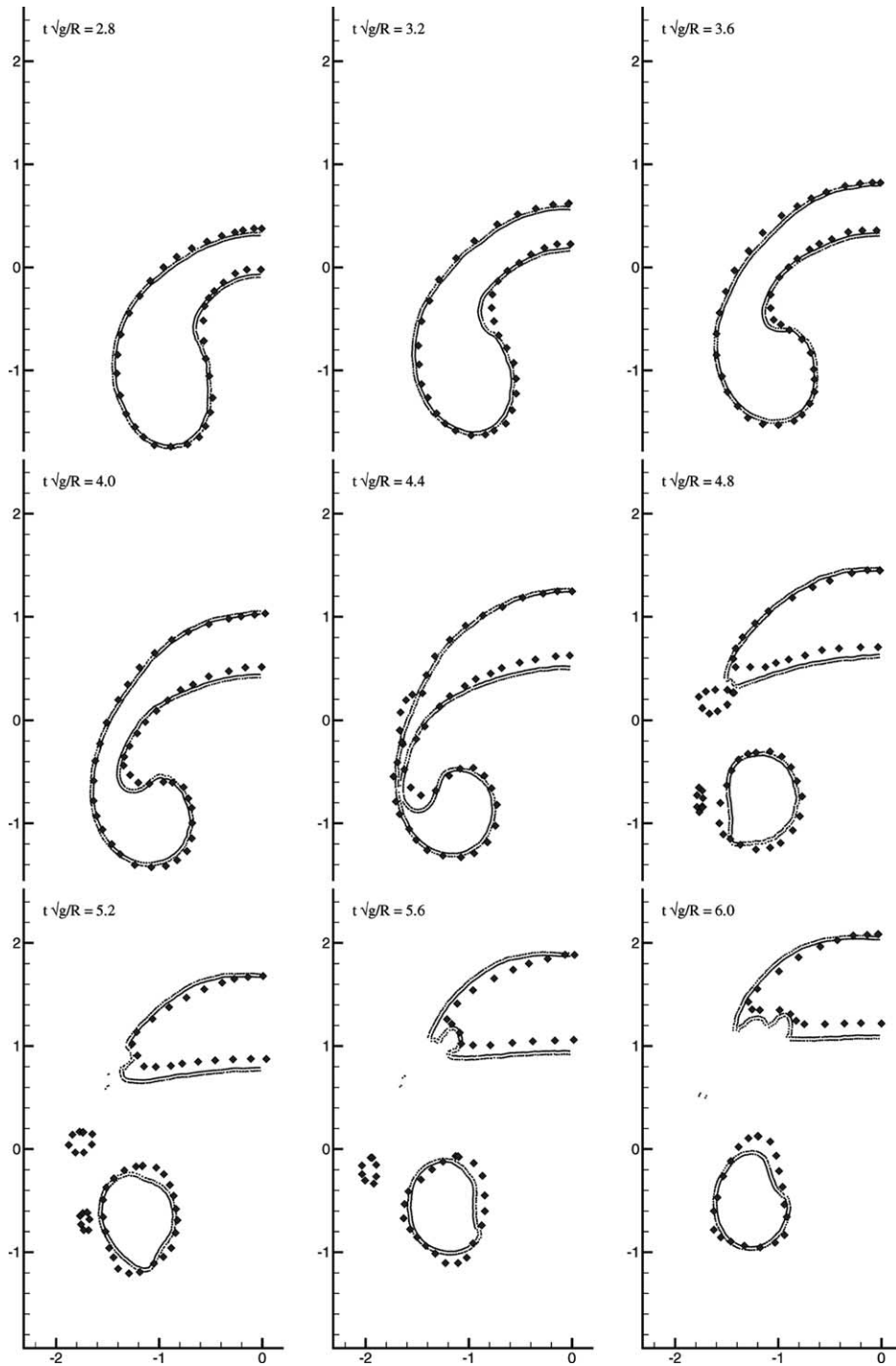


Fig. 6. Rising-bubble problem (cf. Fig. 1),  $\rho_Y/\rho_X = 0.001$ , time increases from left to right and from top to bottom. The red dots are the Level-Set solution from [37] and compared with the present SPH method (black dots). Density re-initialization (14) and (15);  $v = 20$ ; artificial viscosity (18)–(20) with  $\alpha = 0.02$ ; interface-sharpness control with  $\bar{a}\rho_Y^2/\rho_X gR = 1.5$ .

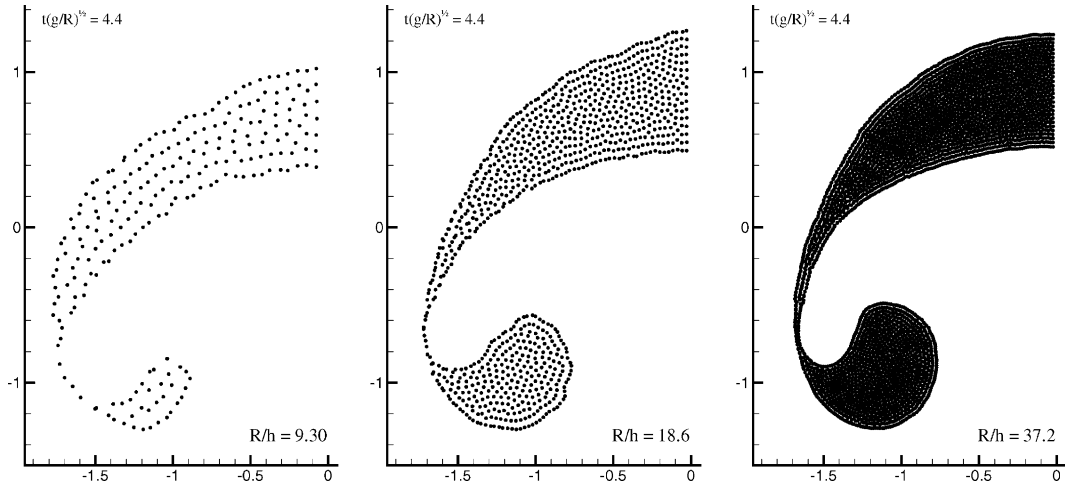


Fig. 7. Convergence test for the rising-bubble problem. The smoothing length  $h$  decreases from left to right.  $\rho_Y/\rho_X = 0.001$ . Ending time of simulation  $\tau = 4.4$ .

Table 1

Convergence test for the rising-bubble problem (ending time of simulation  $\tau = 4.4$ )

$f$	$\varepsilon(f, N, 4N, \tau)$	$\varepsilon(f, 4N, 16N, \tau)$	ord
Thickness	0.0731	0.0382	0.9364
Area	0.0484	0.0047	3.3636
$Y_b$	0.0139	0.0104	0.4111
$V_b$	0.0357	0.0216	0.7232
$E_K$	0.0983	0.0312	1.6576
$E_P$	0.0413	0.0045	3.2139

bubble particles, center of mass velocity  $V_b$  and the total kinetic  $E_K$  and potential  $E_P$  energies of the whole fluid system.

Beside the modified form of the interaction terms, many modifications have been implemented in the present version of our SPH algorithm to obtain the above result. In the following paragraphs, we describe in details these new elements.

**Density re-initialization** In the SPH method, each particle has a fixed mass  $m_j$  and, if the number of particles is constant, mass conservation is intrinsically satisfied. On the other hand, by using the evolution equation for the density, cf. the first equation of (1), we cannot enforce exactly the consistency between mass, density and occupied area (see p. 272 in [3] and [20,27]) as it would be possible by using

$$\rho_i = \sum_j m_j W_{ij}. \quad (13)$$

To alleviate this problem, the density field is periodically re-initialized by applying Eq. (13). In this procedure, special attention has to be paid to the used kernel. In fact, if  $\sum_j W_{ij} \neq 1$  at point  $\mathbf{x}_i$ , the use of (13) would introduce additional errors. In particular, this happens when approaching any boundary of the fluid domain (free surface, interfaces between phases, solid boundaries). In these cases, indeed, the number of particle neighbors seen by a boundary particle decreases, consequently the density computed is smaller than the original value. The equation of state would therefore predict a wrong pressure value and the entire field would be progressively corrupted [21].

In [2], a first-order accurate interpolation scheme on irregularly scattered points has been proposed. Here, we use that approach to re-initialize the density field as

$$\langle \rho_i \rangle = \sum_j \rho_j W_j^{\text{MLS}}(\mathbf{x}_i) dV_j = \sum_j m_j W_j^{\text{MLS}}(\mathbf{x}_i), \quad (14)$$

where the moving-least-square kernel  $W_j^{\text{MLS}}$  is computed through

$$\begin{aligned} W_j^{\text{MLS}}(\mathbf{x}_i) &= [\beta_0(\mathbf{x}_i) + \beta_1(\mathbf{x}_i)(x_i - x_j) + \beta_2(\mathbf{x}_i)(y_i - y_j)] W_{ij}, \\ \boldsymbol{\beta}(\mathbf{x}_i) &= \begin{pmatrix} \beta_0 \\ \beta_1 \\ \beta_2 \end{pmatrix} = \mathbf{A}^{-1}(\mathbf{x}_i) \begin{bmatrix} 1 \\ 0 \\ 0 \end{bmatrix}, \\ \mathbf{A}(\mathbf{x}_i) &= \sum_j W_j(\mathbf{x}_i) \tilde{\mathbf{A}}_{ij}, \\ \tilde{\mathbf{A}}_{ij} &= \begin{bmatrix} 1 & (x_i - x_j) & (y_i - y_j) \\ (x_i - x_j) & (x_i - x_j)^2 & (y_i - y_j)(x_i - x_j) \\ (y_i - y_j) & (y_i - y_j)(x_i - x_j) & (y_i - y_j)^2 \end{bmatrix}. \end{aligned} \quad (15)$$

This procedure is applied every, say,  $\nu$  time steps and increases slightly the computing time, mainly because of the inversion of the  $3 \times 3$  matrix  $\mathbf{A}$  for each fluid particle  $\mathbf{x}_i$ . On the other hand, not only the consistency between mass, density and occupied area is restored, but the results presented in the following show that: (i) a more regular pressure distribution can be obtained and (ii) the total energy is better conserved when artificial viscosity is used in the computations. These benefits have been observed both for free-surface and for interface flows.

The evolution of the pressure field for the free-surface dam-break flow is presented in Fig. 8. Two time instants are shown, respectively before and after the impact of the water front against the vertical wall at the

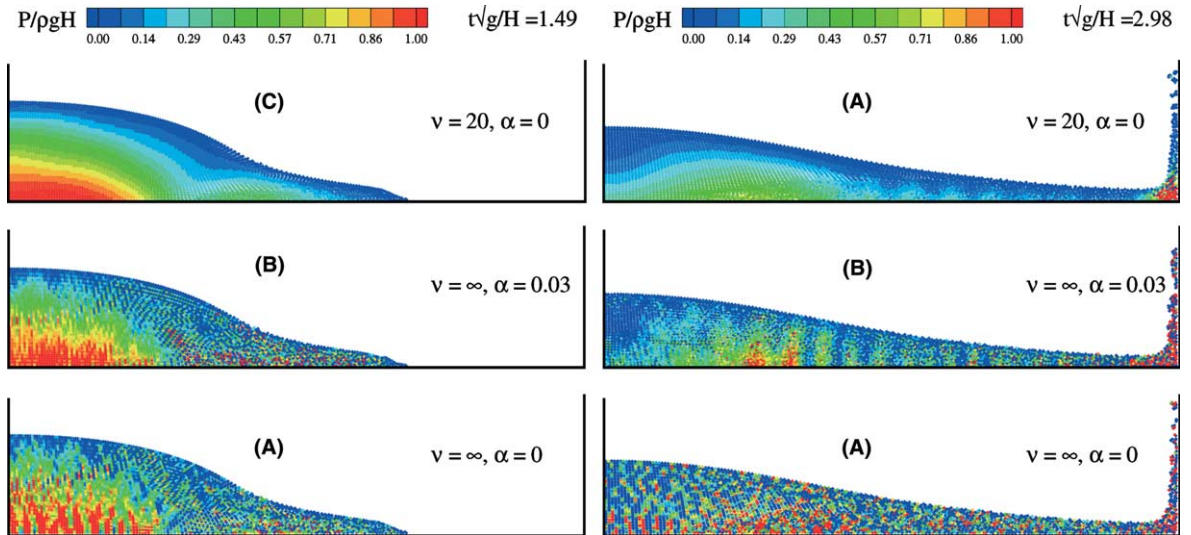


Fig. 8. Free-surface flow generated by the break of a dam. Effect of the periodic density re-initialization on the pressure field (time increases from left to right). The solutions are obtained by the present (12) with (A)  $\nu = \infty$  and  $\alpha = 0$ ; (B)  $\nu = \infty$  and  $\alpha = 0.03$ ; (C)  $\nu = 20$  and  $\alpha = 0$ .

end of the initially dry deck. The solution (A) is obtained without density re-initialization,  $\nu = \infty$ , and turning off the artificial viscosity. Details on the artificial viscosity are discussed in the next section. The solution (B) is obtained without the density re-initialization and by using the artificial viscosity ( $\alpha = 0.03$ , cf. Eq. (18)). Finally, for solution (C) we used the density re-initialization every  $\nu = 20$  time steps and without the artificial viscosity. Although the gross features, e.g. the free-surface profile, of the three solutions are practically the same, it is apparent the growth of high-frequency pressure oscillations in solution (A), which progressively destroy the pressure field, making difficult its physical interpretation and its possible practical use. Moreover, negative values of the pressure possibly attained during such oscillations can trigger tension-instability phenomena [38]. This may cause the computations to stop and in general produce the (unphysical) fragmentation of the water jets during the later overturning.

These spurious oscillations, and their consequences, can be significantly reduced by inserting an artificial viscous term in the momentum evolution equation, as the solution (B) shows. A closer inspection of the pressure field near the bottom right corner, where the pressure gradients are larger, still reveals fluctuations on spatial scale of the order of particle distance. Moreover, when using fictitious viscous terms, the total energy of the system is not conserved, which may be not acceptable when physical time scales long relative to the energy-dissipation rate are of interest. In solution (A), the total energy is conserved up to the machine precision, as expected from the theoretical point of view (a simple proof valid for unbounded flows is given for instance in [3]).

In solution (C), the density re-initialization is applied every  $\nu = 20$  time steps without using the artificial viscosity. Also in this case, we found that the total energy is conserved within the machine accuracy. The pressure field maintains a smooth character, even on a longer time scale, as shown in Fig. 9 where the solution (C) is presented before,  $t(g/H)^{1/2} = 5.95$ , and after,  $t(g/H)^{1/2} = 6.1$ , the impact of the backward plunging jet formed at the end of the run up-run down cycle.

An enlarged view of the free-surface profile for  $t(g/H)^{1/2} = 5.95$  is presented in Fig. 10. The solutions (A), (B) and (C) are compared with the reference solution (dashed line) obtained by a boundary element

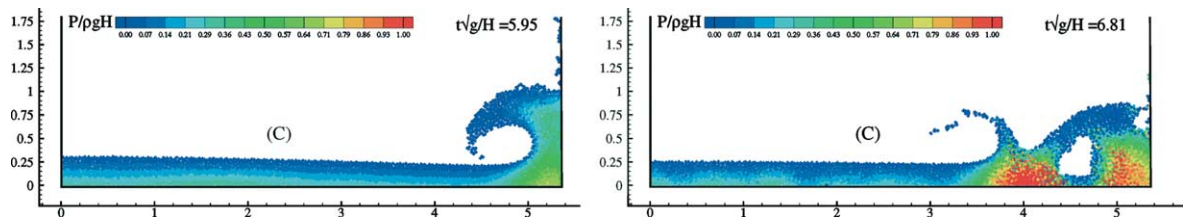


Fig. 9. Free-surface flow generated by the break of a dam. Pressure field (time increases from left to right). obtained by the present (12) with the use of density re-initialization,  $\nu = 20$ , and without artificial viscosity.

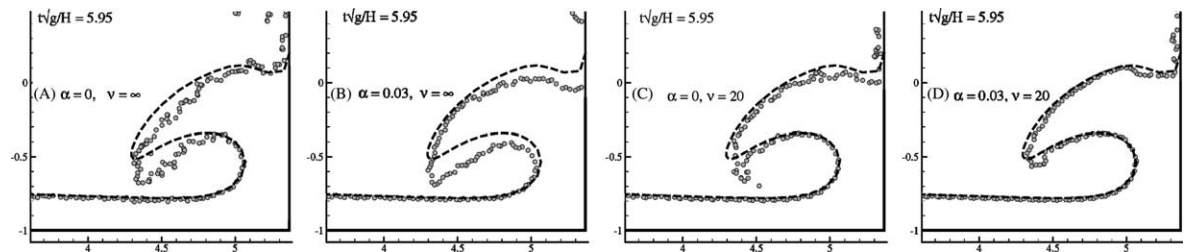


Fig. 10. Free-surface flow generated by the break of a dam. Effect of combined use of density re-initialization and of artificial viscosity on the free-surface definition. The solutions are obtained by the present (12) with: (A)  $\nu = \infty$  and  $\alpha = 0$ ; (B)  $\nu = \infty$  and  $\alpha = 0.03$ ; (C)  $\nu = 20$  and  $\alpha = 0$ ; (D)  $\nu = 20$  and  $\alpha = 0.03$ . The dashed lines are the BEM solution from [12].

method [12]. As anticipated, for  $\nu = \infty$  and  $\alpha = 0$ , the free surface loses its definition and the agreement with the BEM solution is rather poor around the jet region. Though the use of the artificial viscosity keeps the free surface more sharply defined, the agreement is not recovered because the energy dissipation causes the jet to anticipate its downward motion. The density re-initialization improves significantly the solution, though the tip is slightly fragmented and the free surface is less regular than in solution (B). This suggested a combined use of density re-initialization and artificial viscosity, as shown in the rightmost diagram, solution (D), where the good agreement with the BEM solution is apparent.

We now show that the energy dissipation due to the artificial viscosity is significantly reduced when used in combination with the density re-initialization. Therefore it can be used with a negligible effect on the accuracy of long-time simulations. This is not un-expected because the (artificial) energy dissipation is mainly associated with the damping of high-frequency pressure oscillations, which in the present implementation disappear through the periodic use of (14), which may be interpreted as a spatial filter. For the solutions (A)–(D), the left diagram in Fig. 11 shows the time evolution of the total energy

$$E_{\text{TOT}} = \int \frac{1}{2} \rho |\mathbf{u}|^2 dV + \int \rho g y dV + \int \rho e dV, \quad (16)$$

where the last term is introduced to account for the fluctuation of the internal energy  $e$  associated with the (weak) compression of the fluid. To the purpose, the (discretized) evolution equation of the internal energy

$$\frac{De}{Dt} = -\frac{p}{\rho} \text{div} \mathbf{u} \quad (17)$$

is integrated in time, although not entering explicitly into the actual evolution of the particles (the equation of state does not depend on  $e$ ). The total energy is made non-dimensional by the potential-energy imbalance  $\Delta E = E_{p0} - E_{pf}$  corresponding to the static configurations before the dam break,  $E_{p0}$ , and with the same amount of fluid uniformly distributed along the horizontal bottom,  $E_{pf}$ , sketched in the center plot of the same figure. As anticipated, solutions (A) and (C) conserve exactly the total energy. Solution (B) shows a good energy conservation as far as the fluid impacts against the vertical wall, placed at the right end of the dry horizontal bottom. From the impact instant on, marked by (1) in the energy diagram, the conservation of energy deteriorates greatly. The impact of the backward plunging jet, marked by (2), is accompanied by a further increase of the energy-dissipation rate. This is not the case of solution (D) which, in spite of using the artificial viscosity, is characterized by a much smaller and practically constant time rate of energy dissipation during the whole simulation. We mention that the same results on the energy conservation have been obtained by directly computing the work of the artificial viscous terms. Here, we preferred explicitly using (16) to have a heuristic check also in cases with  $\alpha = 0$ .

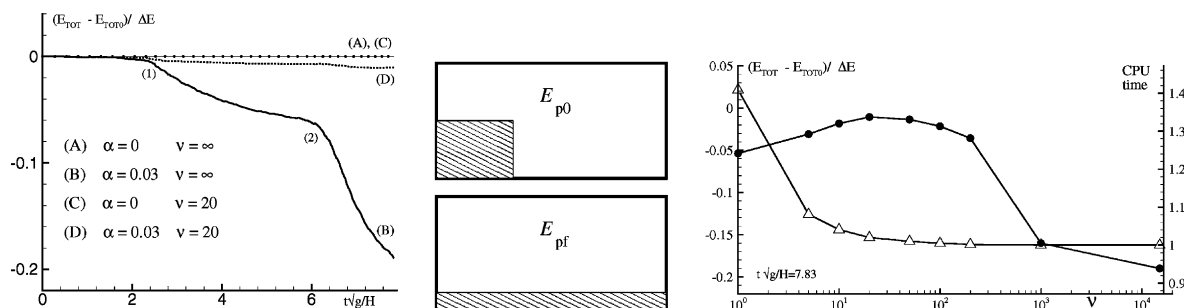


Fig. 11. Free-surface flow generated by the break of a dam. Left: total energy conservation for solutions (A)–(D), cf. caption of Fig. 10. Effect of the interval  $\nu$  of density re-initialization on the total-energy conservation (●) and on the CPU-time per time step (Δ).

For the same test case and solution (D), the right diagram in Fig. 11 shows the effect of the frequency of the density re-initialization on  $E_{\text{TOT}}$  at the end of the simulation  $(t(g/H)^{1/2} = 7.83)$ . In abscissa,  $\nu$  is the interval between two successive application of (14). When  $\nu = \infty$  the re-initialization is never performed, while for  $\nu = 1$  the evolution equation for the density is not used and equation (13) is applied with the moving-least-square kernel. Starting from  $\nu = \infty$ , as  $\nu$  diminishes the energy conservation improves. We found heuristically that optimal values of  $\nu$  are in the range 20–50. We observed that this behavior is qualitatively general, even for completely different problems, and in our simulations we usually adopt  $\nu = 20$ . In the same diagram, the CPU time per time-step is also reported. Values are made non-dimensional by using the CPU time corresponding to  $\nu = \infty$ . As expected, the smaller  $\nu$  is, the longer the CPU time requested is, although for the values of  $\nu$  practically adopted this increment is of the order of 2%.

Finally, we mention that similar benefits could have been obtained by using different interpolation techniques on scattered points than (14) and (15). In [6], the present moving-least-square technique and the lower-order Shepard interpolation have been applied. We have eventually chosen the former for the (slightly) better conservation of total energy.

**Artificial viscous terms** In the practical implementation, a viscous term of the form

$$\Pi_{ij} \nabla W_j(\mathbf{x}_i) dV_j$$

is included in the discretized momentum equation with the purpose to increase the stability properties of the numerical algorithm. We started adopting the form

$$\Pi_{ij} = \begin{cases} -\alpha \mu_{ij} \frac{c_{s,j} + c_{s,i}}{\rho_j + \rho_i} & \text{if } (\mathbf{u}_i - \mathbf{u}_j) \cdot (\mathbf{x}_i - \mathbf{x}_j) < 0, \\ 0 & \text{otherwise,} \end{cases} \quad (18)$$

proposed by Monaghan and Gingold (see the discussion in [20]) where the speed of sound  $c_s$  follows from the state equation. In the present implementation, the original form

$$\mu_{ij} = h \frac{(\mathbf{u}_j - \mathbf{u}_i) \cdot (\mathbf{x}_j - \mathbf{x}_i)}{|\mathbf{x}_j - \mathbf{x}_i|^2 + \varepsilon h^2} \quad (19)$$

has been modified into

$$\begin{aligned} \mu_{ij} &= h \frac{k_j + k_i}{2} \frac{(\mathbf{u}_i - \mathbf{u}_j) \cdot (\mathbf{x}_i - \mathbf{x}_j)}{|\mathbf{x}_i - \mathbf{x}_j|^2 + \varepsilon h^2}, \\ k_i &= \frac{|\text{div} \mathbf{u}_i|}{|\text{div} \mathbf{u}_i| + \sqrt{\mathbf{E}_i : \mathbf{E}_i} + 10^{-4} c_i / h}, \end{aligned} \quad (20)$$

which is an extension of the form

$$k_i = \frac{|\text{div} \mathbf{u}_i|}{|\text{div} \mathbf{u}_i| + |\text{curl} \mathbf{u}_i| + 10^{-4} c_i / h}, \quad (21)$$

proposed by Balsara and reported in [3]. In particular, Balsara has shown that for pure shear flows the use of (21) reduces the generation of spurious entropy. A more general representation of the straining motion is given through the (time) rate-of-strain tensor  $\mathbf{E} = \text{sym}(\nabla \mathbf{u})$ . Therefore, in (20) we have replaced  $|\text{curl} \mathbf{u}_i|$  with the invariant  $\mathbf{E} : \mathbf{E}$  of the rate-of-strain tensor at point  $\mathbf{x}_i$  which corrects the damping in regions of the velocity field with rotation, i.e., related to skew( $\nabla \mathbf{u}$ ). An example is given by further considering the dam-break problem, cf. Fig. 3. Left plot in Fig. 12 shows the interface configuration when the plunging breaker hits the underlying water. The reference solution (solid line) obtained by a boundary-element method [12] is compared with the present SPH implementation. In one case,  $\Delta$ , the artificial viscosity (18) is used with

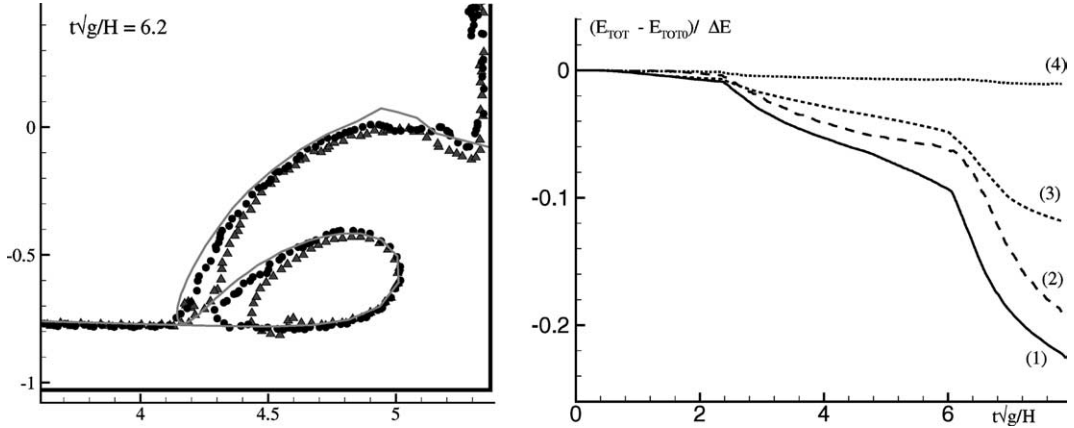


Fig. 12. Free-surface flow generated by the break of a dam. Left: present free-surface SPH simulations are compared with the inviscid free-surface computation by boundary element method (solid line). ( $\Delta$ ) Eq. (19) is used. ( $\bullet$ ) Eq. (20) is used. Right: total-energy conservation; (1) with Eq. (19) and  $\nu = \infty$ ; (2) with Eq. (20) and  $\nu = \infty$ ; (3) with Eq. (19) and  $\nu = 20$ ; (4) with Eq. (20) and  $\nu = 20$ . For all the SPH simulations  $\alpha = 0.03$  has been used (cf. Eq. (18)).

Eq. (19), while the second,  $\bullet$ , adopts the form (20). Apparently, the latter is much closer to the inviscid boundary-element method solution. The reason can be traced back to the high shear which develops near the loop of the breaking front and triggers a too severe artificial damping of the solution when the artificial viscosity (19) is used. Ultimately, this results in an earlier impact of the plunging breaker.

The right diagram shows that the combined use of density re-initialization and Eq. (20) for the artificial viscosity improves the total energy conservation. In general, we found the use of (20) improves the quality of the solution both for free-surface and interfacial flows, and therefore it is usually adopted, unless otherwise stated. From a practical view point, we note that the evaluation of  $k_i$  increases the computational time because of the need to go through the particle list.

For multi-phase flows, the quantities entering in (18) are computed separately within each fluid species. This means that quantities related to particles of the fluid, say,  $Y$  are computed without considering the presence of  $X$ -fluid particles even when they are close to the interface.

We note that the equivalent kinematic viscosity associated with  $\Pi_{ij}$  has the form  $\alpha c_s h$  [22]. In our simulations the influence of  $\alpha$  has been checked in the range 0.005–0.03.

### 2.3.1. XSPH correction

To prevent particles inter-penetration, and to regularize the weakly compressible treatment of liquids, Monaghan introduced the XSPH velocity-correction  $\Delta \mathbf{u}_i$ , which takes into account the neighbors velocities through a mean velocity evaluated within the particle support, i.e.,

$$\langle \mathbf{u}_i \rangle = \mathbf{u}_i + \Delta \mathbf{u}_i, \quad \Delta \mathbf{u}_i = \frac{\varepsilon}{2} \sum_j \frac{m_j}{\bar{\rho}_{ij}} (\mathbf{u}_j - \mathbf{u}_i) W_{ji}, \quad \bar{\rho}_{ij} = \frac{\rho_i + \rho_j}{2}. \quad (22)$$

The corrected velocity  $\langle \mathbf{u}_i \rangle$  is used in density and position evolution equations and not in the momentum equation. For two-phase flows, when the particle  $i$  is near the interface, the corresponding mean density  $\bar{\rho}_{ij}$  is wrongly evaluated and the XSPH correction leads to wrong results. In our implementation, when considering one medium, the XSPH correction is computed without considering influence of the other media possibly present.



Moreover, the divergence operator is used in the form

$$\operatorname{div}(\mathbf{u}_i) = \sum_j (\mathbf{u}_j - \mathbf{u}_i) \cdot \nabla W_{ji} \frac{m_j}{\rho_j} + \sum_j (\Delta \mathbf{u}_j - \Delta \mathbf{u}_i) \cdot \nabla W_{ji} \frac{m_j}{\rho_j}. \quad (23)$$

For free-surface flows, with some exceptions, the correction of the divergence is often negligible [21]. In our experience, when studying two-phase flows this correction is large and its use improves significantly the accuracy of the solution, as demonstrated in Fig. 13. Further, the energy conservation was always found (graphically) unaffected by the use of the XSPH correction, both for free-surface and for two-phase flows. From a computational point of view, the second term in (23) implies to go through the whole list of particles, increasing the computational cost.

### 2.3.2. Control of interface sharpness

As discussed in [13], the use of the pressure gradient in the form (7) implies fictitious surface-tension effects which are not detected in the present implementation. On the contrary, by the present formulation, we observed the fragmentation of the bubble and, for small density ratios, the dispersion of the light fluid in the heavier one, cf. the right plot of Fig. 13. To keep the interface sharp, the state equation has been modified as

$$p(\rho) = P_0 \left[ \left( \frac{\rho}{\rho_0} \right)^\gamma - 1 \right] + \chi - \bar{a} \rho^2, \quad (24)$$

where the last term models a cohesion force, as suggested in [29]. The pressure gradient becomes

$$\nabla p_i = \sum_j (p_j + p_i) \nabla W_j(\mathbf{x}_i) dV_j - \bar{a} \sum_j (\rho_j^2 + \rho_i^2) \nabla W_j(\mathbf{x}_i) dV_j. \quad (25)$$

In the present computations, the modified state equation has been used only for the lighter fluid  $Y$ , and the last term of Eq. (25) can be written as

$$-\bar{a} \sum_{j \in Y} (\rho_j^2 + \rho_i^2) \nabla W_j(\mathbf{x}_i) dV_j. \quad (26)$$

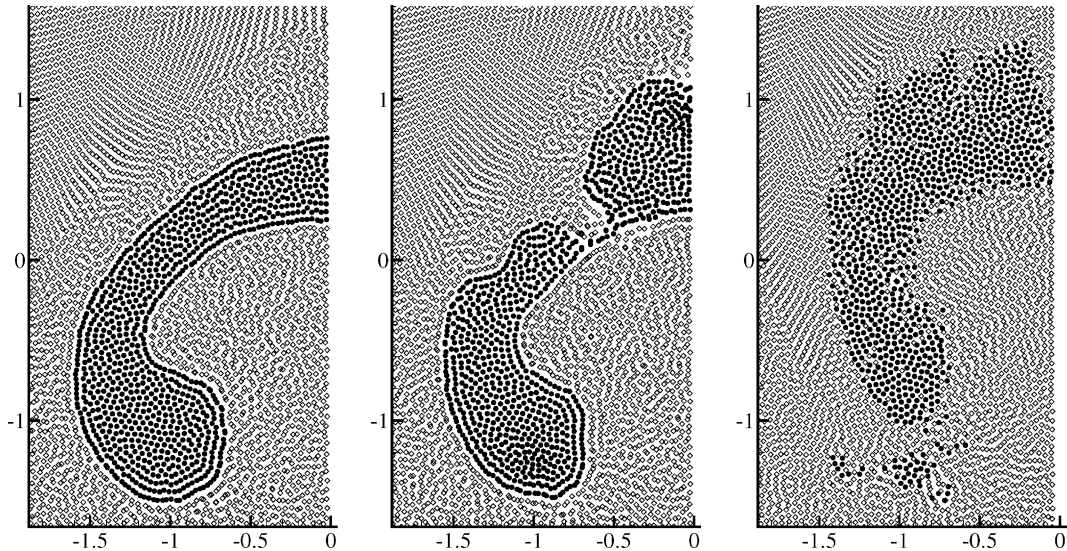


Fig. 13. Bubble of fluid  $Y$  rising through the heavier fluid  $X$ ,  $\rho_Y/\rho_X = 0.001$ . Left: present SPH implementation for  $t(g/R)^{1/2} = 3.6$ . Center: same case without using the modified divergence (23). Right: same case without Eq. (25).

For the purpose of discussion, we note that (26) can be approximated as

$$-2\bar{a}\rho_{0Y}^2 \sum_{j \in Y} \nabla W_j(\mathbf{x}_i) dV_j. \quad (27)$$

Because of the kernel properties, the sum in (27) is (practically) zero for a particle  $j$  totally embedded within its own phase and results in a vector normal to the interface as the particle approaches it. The parameter  $-\bar{a}$  controls the strength of the cohesion force.

In the present paper, no attempt has been made to model physical surface-tension effects, either by using the modified state equation (24) or by the approach suggested in [28] based on the evaluation of the curvature at the interface.

### 2.3.3. State equation

In the present implementation, we use the state equations

$$p_X(\rho) - \chi = P_{0,X} \left( \left( \frac{\rho}{\rho_{0,X}} \right)^{\gamma_X} - 1 \right), \quad p_Y(\rho) - \chi = P_{0,Y} \left( \left( \frac{\rho}{\rho_{0,Y}} \right)^{\gamma_Y} - 1 \right), \quad (28)$$

and the corresponding sound speeds are

$$c_X = \sqrt{\frac{P_{0,X}\gamma_X}{\rho_{0,X}}}, \quad c_Y = \sqrt{\frac{P_{0,Y}\gamma_Y}{\rho_{0,Y}}}. \quad (29)$$

For the water–air interface, typical adopted values are  $\gamma_X = 7$  and  $\gamma_Y = 1.4$ , respectively. The reference pressure  $P_0$  is usually chosen to achieve a small compressibility for the  $X$ -phase, that is  $U_{X,\max}/c_X \ll 1$  where  $U_{X,\max}$  is the expected order of magnitude of the fluid velocity for the considered problem. We note that both (7) and (11) imply that for a uniform non-zero pressure the exchanged force between the particles is non-zero. Therefore, the chosen form of the state equation ensures that for  $\rho(\mathbf{x}) = \rho_0$  the pressure is zero and the fluid stays at rest.

From Eq. (29), we note that for small density ratio  $\rho_Y/\rho_X$  the sound speed in the phase  $Y$  is much larger than in the heavier phase, and therefore the compressibility is relatively smaller in, say, air than in water. Typical state diagrams practically adopted are shown in Fig. 14 for  $\chi = 0$ . It is evidenced that to operate in the same pressure range (as needed by the dynamic condition at the interface) the lighter fluid  $Y$  needs to be modeled by a steeper state curve, hence with a higher sound speed. In the computational practice, since the method stability is related to the speed of sound, as the density ratio decreases the time step  $\Delta t$  decreases largely to prevent unstable evolutions in the lighter phase.

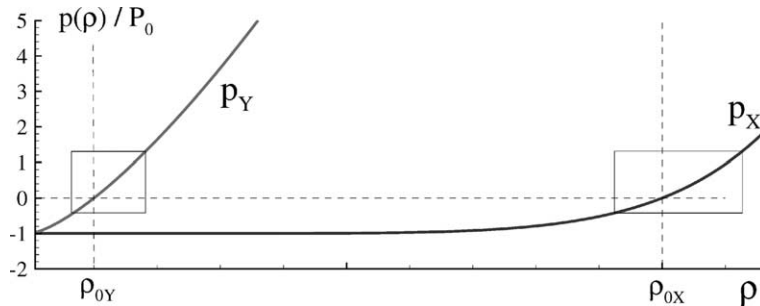


Fig. 14. State-equation diagrams for the two phases showing that to operate in the same pressure range the lighter fluid needs a steepest density–pressure characteristic curve.

### 2.3.4. Time-stepping scheme

The computations here reported have been obtained by using a fourth-order Runge–Kutta scheme, with dynamic choice of the time step  $\delta t$  to satisfy a Courant Friedrichs Levy-type condition. In our experience, we found that the stability properties of this scheme are better than modified-Euler and Leap–Frog schemes and that larger time steps can be used, reducing the total computational time. Conversely, for the same  $\delta t$ , the accuracy of the solution increases at the expenses of larger CPU time. The adopted CFL condition

$$\delta t = \beta \min_j \left( \frac{h}{c_{s,i} + \sigma_i} \right), \quad \sigma_i = \max_j \left| h \frac{(\mathbf{u}_j - \mathbf{u}_i) \cdot (\mathbf{x}_j - \mathbf{x}_i)}{|\mathbf{x}_j - \mathbf{x}_i|^2} \right| \quad (30)$$

has been proposed in [25]. In (30),  $c_{s,i}$  is the speed of sound of the  $i$ th particle. The minimum is evaluated over all neighbors of the  $i$ th particle and the maximum over all the particles contributing to (18)–(20). In our experience, the constant  $\beta$  is about 2.5 for the fourth-order Runge–Kutta scheme and 0.3 for the modified Euler scheme.

### 2.3.5. Free-slip condition on solid boundaries

Throughout this paper, the considered flow fields are confined within fixed solid boundaries over which a free-slip condition is enforced. A possible approach to enforce the no-penetration (or more general) boundary condition in SPH computations is using “repellent” particles [21,25].

Differently, we propose to mimic the body by “ghost particles” with density, pressure and velocity deduced from those of the physical particles adjacent to the solid boundary. Let us consider a plane wall, as in right plot of Fig. 15. At each time step, all particles within a layer with thickness  $\mathcal{O}(h)$  from the wall are mirrored inside the body. The characteristics given to the ghost particles are

$$\begin{aligned} \mathbf{x}_{iG} &= 2\mathbf{x}_w - \mathbf{x}_i, & \mathbf{u}_{niG} &= 2U_{nw} - \mathbf{u}_{ni}, & p_{iG} &= p_i, \\ \mathbf{u}_{tiG} &= \mathbf{u}_{ti}, \end{aligned} \quad (31)$$

where  $(\cdot)_t$  and  $(\cdot)_n$  mean the tangential and normal velocity components to the boundary,  $U_{nw}$  is the local displacement velocity of the rigid boundary with instantaneous position  $\mathbf{x}_w$ . For plane boundaries (31), allow to fulfill exactly the free-slip condition. For arbitrary shaped boundaries, as shown in the left plot, the mirroring is performed pointwise by considering the local tangent plane. Corrections have to be enforced to avoid an excess of ghost-mass. In practice, comparisons with boundary element-method computations in

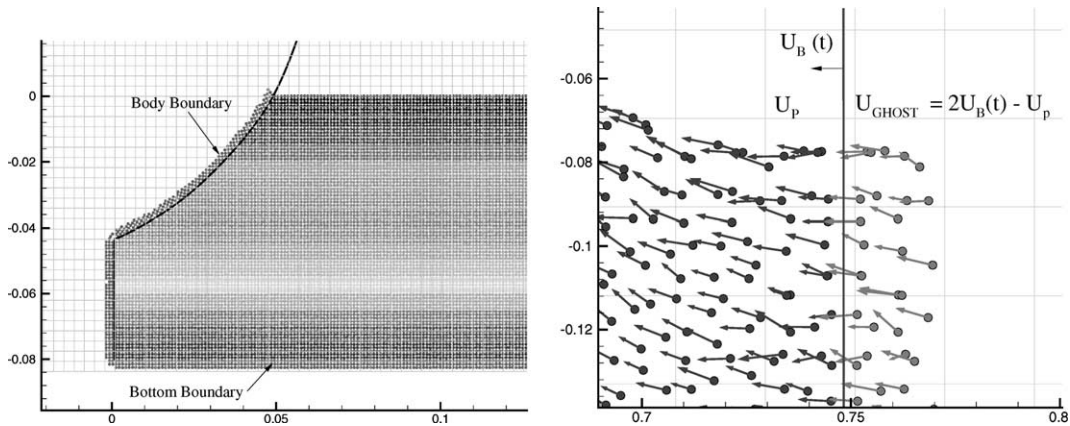


Fig. 15. Ghost particles. Left: example of curved rigid boundary modeled by ghost particles. Right: enlarged view with details of the mirrored velocity field.

case of surface-piercing bodies gave good results [15,16]. Though the repellent-particle approach has probably a larger flexibility, we preferred the ghost-particle approach for the smoother behavior of the particles in proximity of the modeled boundary. We never attempted to enforce a no-slip boundary condition.

### 3. Two-phase modelling of dam-break and impact problems

We discuss the flow originated by the break of a dam and the impact of the water front against a fixed vertical wall, located downstream the dam. In spite of its simplicity, this problem embeds several features related to practical hydrodynamic circumstances, e.g. slamming loads on ship hulls impacting on water surface, green-water loads on deck and deck-structures of marine structures, sloshing loads in tanks [11], or wave loads on coastal structures [31].

#### 3.1. General features

We first study a case without fluid impact, reproducing one of the experiments in [18] ( $L/H = 1$ ,  $H \simeq 5.7$  cm), and previously considered in [21]. In the experiments, the water was initially contained within the solid boundary of a water flume and a piece of wax paper, clamped between two metallic frames. The intense current produced by a short circuit has been used to melt the wax and quickly release the paper diaphragm, leaving the water free to flow along a practically unlimited dry deck.

Left plot in Fig. 16 gives the propagation in time of the water-front toe  $x_{\text{front}}$  after the dam break. The free-surface SPH solution,  $\square$ , is compared with a boundary-element method solution, solid line, and a Navier–Stokes solution,  $\circ$ . The free-surface SPH simulation has been performed with:  $N_X = 6320$ ,  $h/H = 1.3 \times 10^{-2}$ ,  $c_X/(gH)^{1/2} = 10$ ,  $P_{0,X}/\rho gH = 14.3$ . We have used  $\nu = 20$ , and we have verified that results are unaffected for  $\alpha = [0.005 - 0.03]$ . In case of simulation with  $\rho_Y/\rho_X = 0.001$ , the water-front velocity is graphically superimposed to the result for  $\rho_Y/\rho_X = 0$  (cf. also right plot in the same figure), and for this test case the air–water model is not further discussed.

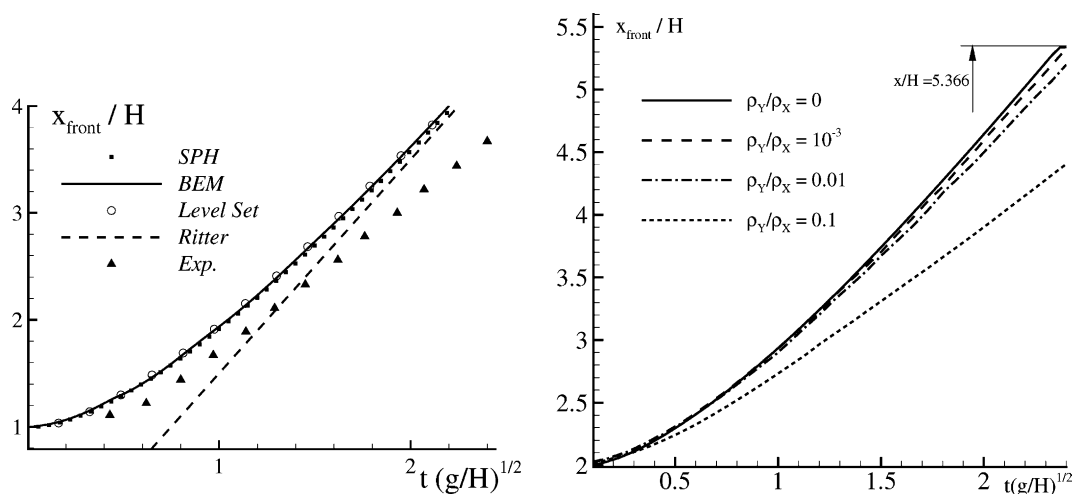


Fig. 16. Time evolution of the water-front toe.  $t = 0$  is the time instant for dam break and  $x_{\text{front}}$  is the position of the water front. Left: test-case from [18]. Right: test-case from [40], the horizontal line indicates the presence of the vertical wall.

All numerical solutions agree very well. The fluid smoothly accelerates and reaches an almost constant value of the velocity. For  $t = 0$ , the inviscid solution would be singular at the contact point between the free surface and the dry deck [32], though none of the methods captures this behavior. As expected, on a longer time scale, the numerical solutions approach the analytical non-dimensional water-front velocity  $v/(gH)^{1/2} = 2$  given by the shallow-water analysis [33]. The latter is not applicable to the initial instants of the phenomenon because shallow-water conditions are not verified, and the water-front location would be largely overestimated with respect to all the reported solutions. Therefore, the Ritter solution has been shifted laterally just to show the tendency of the numerical simulations to approach the shallow-water result after a suitable time interval. The experimental data are characterized by a slower water-front velocity. The comparison between the different numerical solutions and the correct asymptotic behavior are rather convincing that the departure from the experimental results is partly related to experimental uncertainties and partly to physical effects not modeled. For  $t(g/H)^{1/2} < 1$ , the differences between measurements and (all) numerical results may be due to experimental reasons, e.g. non-uniform breaking of the diaphragm. On a longer time scale, the bottom-induced drag alters the propagation velocity and triggers the development of turbulence near the water front and causes the increasing delay between simulations and experiments.

We now go back to the case anticipated in Fig. 3, which reproduces the experiments in [40], where a reservoir of water,  $H = 60$  cm and  $L = 2H$ , is placed at a distance  $L_c = 3.366H$  from a vertical obstacle. The sequence in Fig. 17 shows the global development of the fluid flow for  $\rho_Y/\rho_X = 0$  (the free-surface case), 0.001 (the air–water case) and 0.1, from left to right, respectively. After the dam is removed, the flow develops along the deck, impacting against the vertical wall. The fluid is violently deviated upwards. Formation of spray and fragmentation of the free surface may occur. Though the SPH predicts high particle velocities, and some particles leave the main bulk of the fluid, it is expected that the resolution of these small-scale details is poor. Later, under the restoring action of gravity, the fluid acceleration decreases and the upward-moving jet slows down. The motion of the water is then reversed in a waterfall, overturning in the form of water plunging onto the wetted deck. A cavity is formed, entrapping the lighter fluid in the case of two-phase simulations. Splash up of liquid follows the impact of the plunging breaker. For  $\rho_Y/\rho_X = 0$ , BEM computations and the present SPH computation agree fairly well up to the backward plunging breaker occurred, cf. Fig. 12. A further verification has been provided by comparison with Level-Set computations [8], as reported in Fig. 18. The overall agreement is rather good. Rather small differences are detected in the details of the splash up, of the entrapped cavity and near the intersection with the vertical wall. The Level-Set solution is numerically smoothed. Probably, both SPH and Level-Set computations loose the resolution at the tip of the splash up, where also some fragmentation is predicted by the SPH method.

Qualitatively, the main features of the flow evolution are the same for the different density ratios considered. Before the impact, a quantitative comparison can be made through the propagation of the water front along the horizontal bottom (right plot in Fig. 16), the slope of the water front and its impact velocity against the vertical wall, Fig. 19. The two latter features are those determining the initial impact load and are of practical interest [12]. The limiting case  $\rho_Y/\rho_X = 0$  corresponds to water moving in a vacuum. As expected, the greater the  $Y$ -density is, the more the water motion is impeded. Consequently, the water-front velocity decreases as  $\rho_Y/\rho_X$  increases and seems to reach different asymptotic values. Differences are negligible between the free-surface flow and the air–water case. The slope of the water front (left plot) increases rapidly and the impact velocity (right plot) is smaller and smaller as the weight of the upper fluid increases.

The maximum run up on the vertical wall (left plot in Fig. 20) exceeds always the double of the initial water height of the reservoir, and increases as the density ratio decreases, consistently with the higher impact velocity. For the considered density ratios, the area of the entrapped cavity, right plot, attains a minimum value for  $\rho_Y/\rho_X \simeq 0.01$  and increases both for larger and for smaller density ratios.

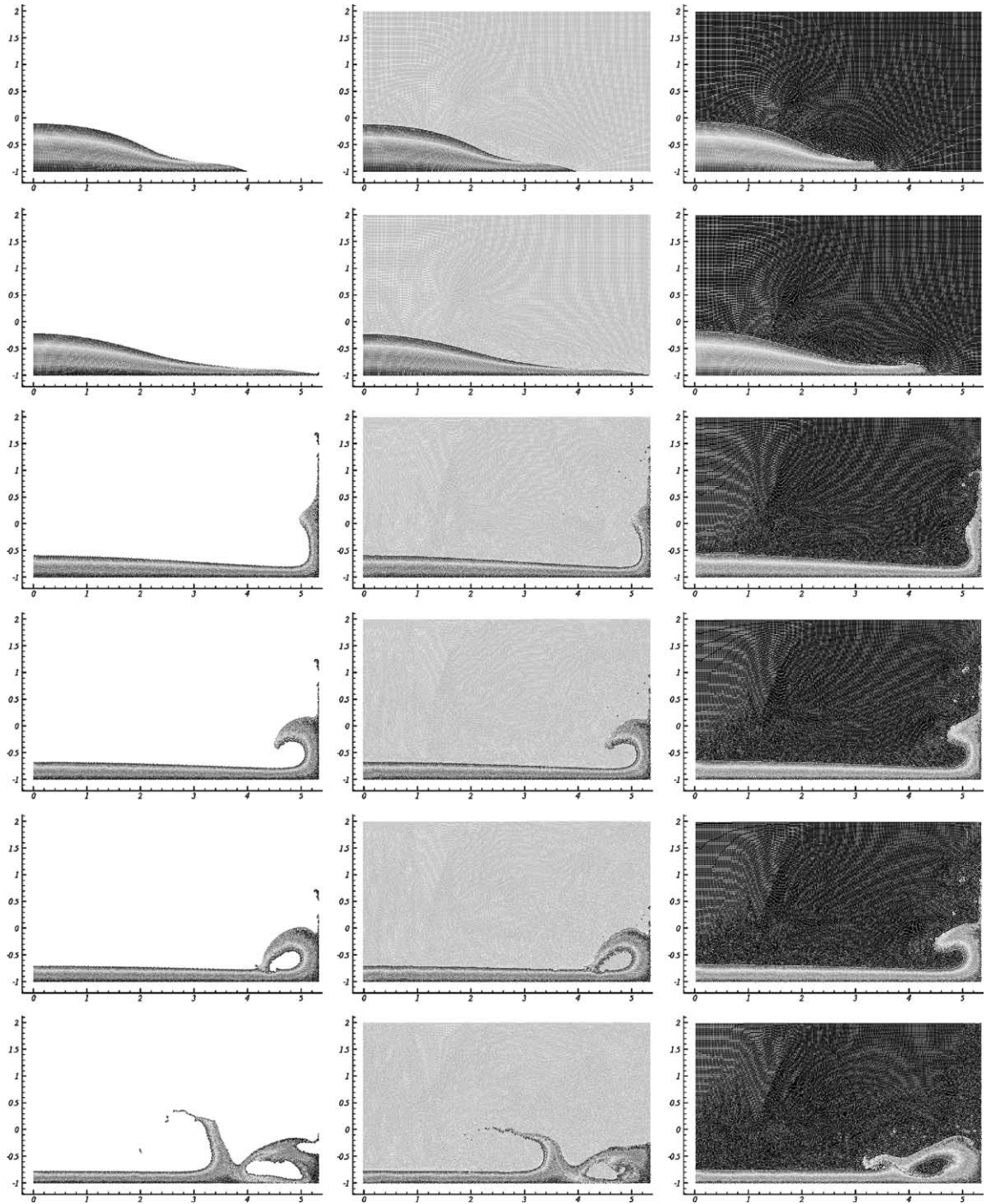


Fig. 17. Dam-break flow and impact against a vertical wall. From left to right,  $\rho_Y/\rho_X = 0, 0.001$  and  $0.1$ , respectively. Time increases from top to bottom:  $t(g/H)^{1/2} = 1.66, 2.04, 4.81, 5.72, 6.17, 7.37$ . The parameters of the numerical simulations are:  $N_X = 4900$ ,  $N_Y = 34172$ ,  $\gamma_X = 7$ ,  $\gamma_Y = 1.4$ ,  $P_{0,X}/(\rho_X g H) = 28.5$ ,  $P_{0,X} = P_{0,Y}$ ,  $h/H = 2.686 \times 10^{-2}$ ,  $\alpha = 0.03$  and  $\nu = 20$ . The  $X$ -data apply to the free-surface flow.

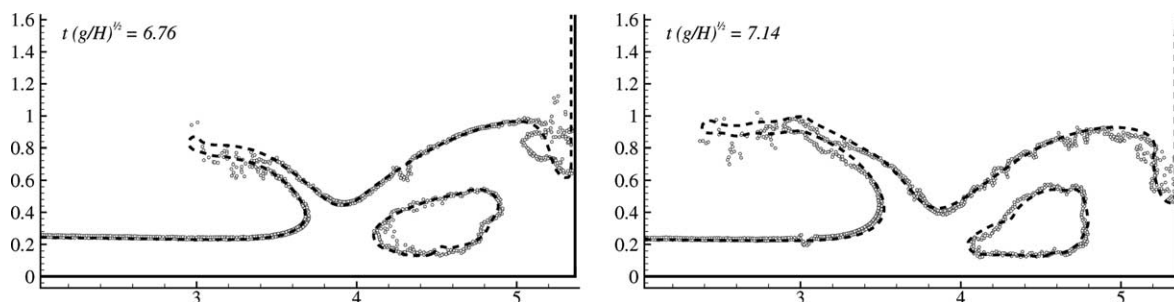


Fig. 18. Dam-break flow and impact against a vertical wall,  $\rho_Y/\rho_X = 0.001$ . Comparison of the present SPH computations with the Level-Set solution (dashed line) of the Navier-Stokes equations from [7,8].

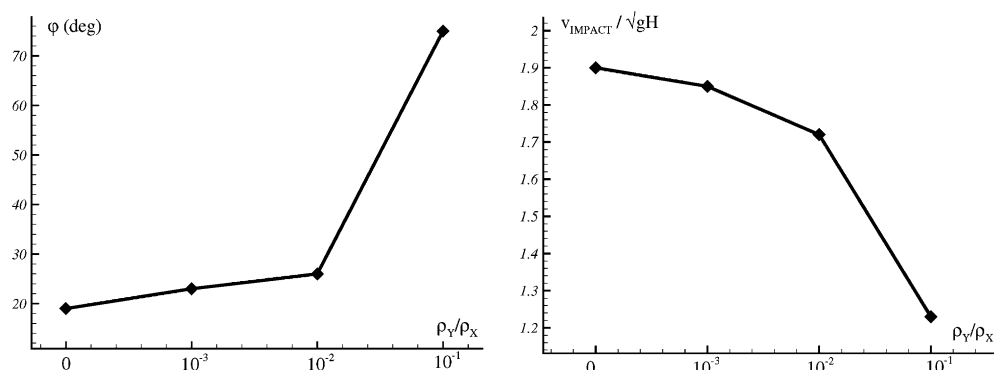


Fig. 19. Dam-break flow and impact against a vertical wall. Effect of density ratio on water-front characteristics. Left: water-front slope. Right: water-front impact velocity.

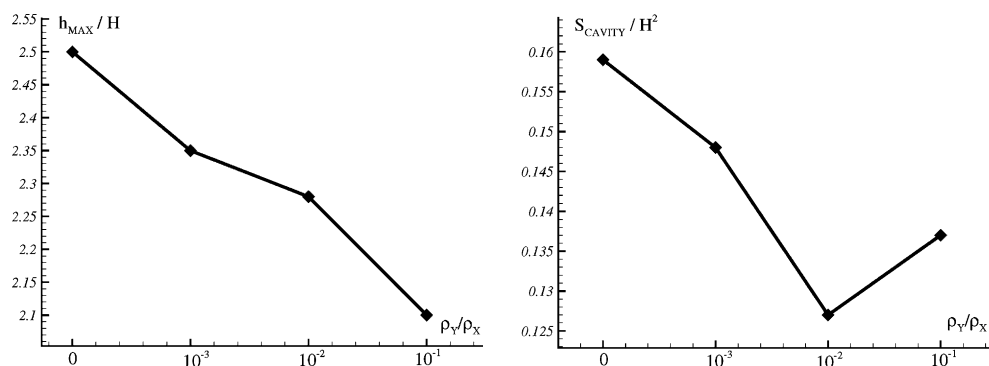


Fig. 20. Dam-break flow and impact against a vertical wall. Left: maximum run up. Right: area of the entrapped cavity.

Fig. 21 gives the time evolution of the water height  $h_1$  and  $h_2$  at locations  $(x/H)_1 = 0.825$  and  $(x/H)_2 = 1.653$ , respectively, from the right vertical wall. The air–water case (solid lines) and the free-surface simulation (dotted lines) are compared with measurements,  $\triangle$ , from [40]. In the experiments, standard capacitive wave gauges have been used which are sensitive to the wetted portion of the wire.



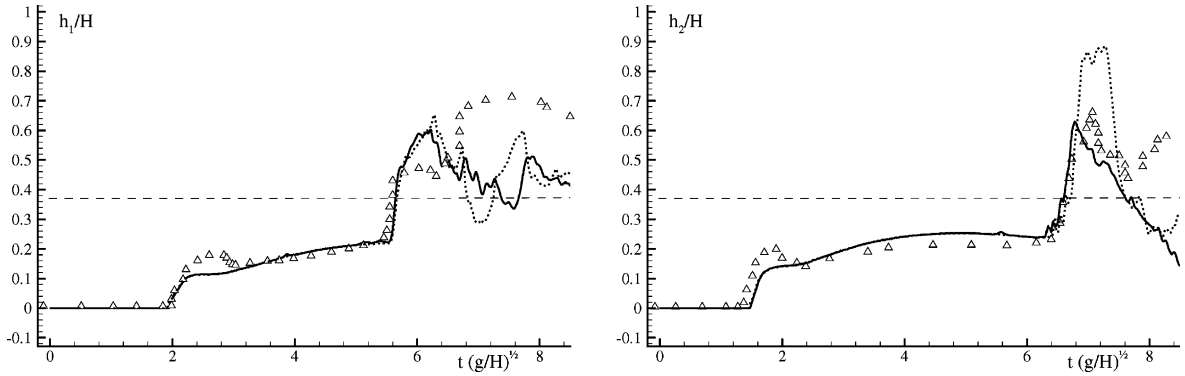


Fig. 21. Total height  $h$  of the water at  $(x/H)_1 = 0.825$  (left) and  $(x/H)_2 = 1.653$  (right). Solid line:  $\rho_Y/\rho_X = 0.001$ ; dotted line:  $\rho_Y/\rho_X = 0$ ; ( $\Delta$ ) experiments from [40].

Hence, the numerical values are deduced from the simulations by taking the water level and deducting the height of the (possibly present) entrapped cavity. The initial evolution,  $t(g/H)^{1/2} \simeq 1.6\text{--}2$ , is characterized by the sudden rise of the water level due to the transition from dry-deck to wet-deck conditions. The water-front shape determines the actual growth rate of  $h$ . Therefore, the differences detected between numerical and experimental data are reasonably due to details of the initial conditions in the experiments and bottom-roughness effects. The two SPH simulations are in agreement, showing a limited role of the air motion at this stage.

As time passes,  $t(g/H)^{1/2} \simeq 2\text{--}5.6$ , a smaller growth rate of the water level is observed, which corresponds to nearly flat interface above the wave gauges. The agreement between measurements and numerical data is still satisfactory.

A second steep increase of  $h$  is then observed due to the water overturning which gives an additional contribution to the water height. This is first seen for  $t(g/H)^{1/2} \sim 5.6$  at the location closest to the wall, and later,  $t(g/H)^{1/2} \sim 6.2$ , recorded by the farther gauge. The agreement of the two-phase modelling with the experiments is rather good, while the free-surface computation largely over-predicts the water height  $h_2$ .

Later on, the experiments and the present simulations largely differ. A Level-Set simulation, not shown, confirms the SPH results but the limited information about the experiments does not allow a better discussion of such comparison.

### 3.2. Air-cushion effect on impact pressure

For a given density ratio, the (inviscid) flow generated by the dam break is governed by Froude scaling [36]. The initial stage of the impact against the vertical wall is then solely controlled by the inertia of the fluid, and the two-dimensional flow is well described in terms of a gravity-less potential flow. Later on, during the run up-run down cycle, the flow is again controlled by the gravity.

As soon as a cavity is formed, the compressibility of the entrapped fluid enters the problem. The following discussion is based on results for the air–water case but varying the ambient-pressure conditions.

Fig. 22 presents the pressure measured on the vertical wall during the impact. In the experiments, a circular shaped gauge of 9 cm ( $\sim 0.15H$ ) diameter has been used, located on the vertical wall with the center  $0.267H$  above the deck. The top-left plot shows the experimental data compared with the numerical values computed at that location. As expected, the impact of the water front against the vertical structure is accompanied by a sudden pressure rise,  $t/\sqrt{gL} \simeq 2.4$ , and both the numerical simulations recover reasonably well the measurements. In this initial stage, pressure and loads mainly depend on velocity and slope of the

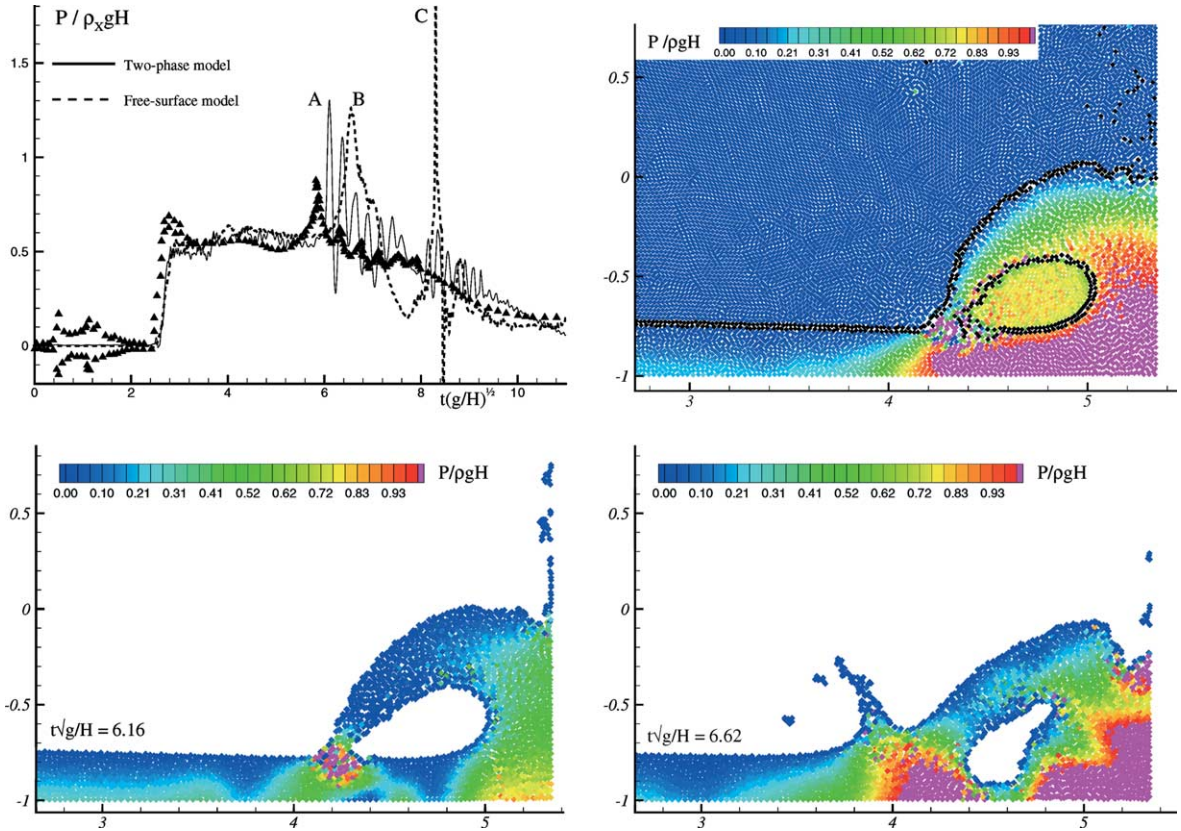


Fig. 22. Dam-break flow and impact against a vertical wall. Top left: pressure evolution on the wall (see text); solid line: two-phase simulation; dashed line: free-surface simulation; (●) experiments from [40]. Top right: air water-flow configuration,  $\rho_Y/\rho_X = 0.001$ , corresponding to the pressure peak A in the pressure evolution. Bottom: free surface-flow configurations corresponding to peaks B and C in the pressure evolution left and right respectively.

impacting water front [9,12], and the overshoot of the experimental data is probably related to details of the experimental conditions and cannot be further commented.

The backward plunging water front induces a second pressure peak on the vertical wall, cf. peak A in Fig. 22. This phenomenon corresponds to the formation of a closed cavity and can be further discussed by means of the corresponding pressure contour in Fig. 22 for  $\rho_Y/\rho_X = 0.001$  and 0 (top-right and bottom-left plots, respectively). In the air–water case, the pressure rise inside the air cavity is felt also in a large water region, near the corner. This air-cushion effect is not observed in the free-surface flow, and an increase of the pressure is localized around the plunger tip impinging on the underlying layer of water. Actually, cf. peak B in Fig. 22, the free-surface simulation shows a delayed pressure rise which can be related with the fast circulatory flow around the entrapped cavity shown in bottom-right plot of Fig. 22. The reliability of the latter result is clearly affected by the lack of modelling of the entrapped air. For  $\rho_Y/\rho_X = 0$ , the final collapse of the empty cavity results in the large pressure peak C which is totally unphysical.

On a longer time scale, the two-phase computation predicts a slow decay of the mean-level pressure which is in reasonable agreement with the experiments. In more details, the numerical results show high-frequency oscillations associated with pulsations of the entrapped air bubble larger than in the experimental record. As discussed in [39], a number of experimental details make rather difficult a precise quantitative comparison with experimental results. In the present case, the number of the available experimental

samples, the frequency-response uncertainty of the transducer adopted, three-dimensional effects and leakage of air do not allow a complete interpretation of the measurements.

For further verification, following [1] and [39], we expect that for short time after its formation the pressure inside the bubble is solely governed by the compressibility of the trapped air. On this ground, for small departures from the initial bubble pressure, the pressure peak  $P_{\max}$  and the rise time  $\tau_{\max}$  should scale as

$$\frac{P_{\max}}{\rho_X V_j^2} \sim \left( \frac{\gamma_Y P_0}{\rho_X V_j^2} \right)^{1/2}, \quad \frac{\tau_{\max} V_j}{S_{\text{cavity}}^{1/2}} \sim \left( \frac{\gamma_Y P_0}{\rho_X V_j^2} \right)^{-1/2}, \quad (32)$$

where  $S_{\text{cavity}}$  is the initial area of the cavity and  $V_j$  the characteristic downward velocity of the water above the bubble. The area  $S_{\text{cavity}}$  area is evaluated when the jet touches the underlying liquid, and the rise time  $\tau_{\max}$  is measured starting from this event on. The definition of  $V_j$  is less precise but different choices do not alter qualitatively the above scaling. For the following results, we have used the mean vertical velocity at the tip of the plunging jet. With these premises, Fig. 23 shows pressure oscillations for a point inside the air bubble trapped by the backward plunging breaker. At the beginning, the pressure field is almost uniform inside the cavity, and the pressure evolution of a single point suffices to describe qualitatively the phenomenon. On a longer time scale, the distortion of the bubble due to the surrounding water motion and buoyancy effects affect the observed evolution. By keeping fixed all parameters, we have modified the compressibility of the upper fluid through  $P_{0,Y}$ . The results in terms of pressure peak and rise time are summarized in the center plot of Fig. 23, where the scaling laws (32) are clearly fulfilled. In the same figure, the right plot shows that the same scaling applies to the rise time and pressure peak on the wall.

It is worth a general comment on the applicability of the present analysis to air-cushion type phenomena. In our formulation, both water and air have been modelled by the same state equations (28), with suitable choice of the coefficients  $\gamma$ . For the water, this results in the weakly compressible approximation. For the air, it can be interpreted as the adiabatic ( $\gamma = 1.4$ ) evolution of a truly compressible gas. This assumption is consistent with Bagnold's analysis, based on the same thermo-dynamic hypothesis and on negligible dynamic effects related to the air motion. The latter are included in our numerical model. Therefore, as far as the scheme of adiabatic evolution of a single bubble of air is able to capture the actual physics, the adopted physical scheme is general enough to be applicable.

Frequently, instead of a single bubble, an air–water mixture is observed. In this case, we could consider a “bubbly phase” inside the region entrapped by the water and using there a suitable state equation. For a mixture of water with small-size bubbles may for instance be preferable to assume an isothermal evolution ( $\gamma = 1.0$ ). A more detailed discussion on the effect of entrained air in cushioning water impact is addressed in [30].

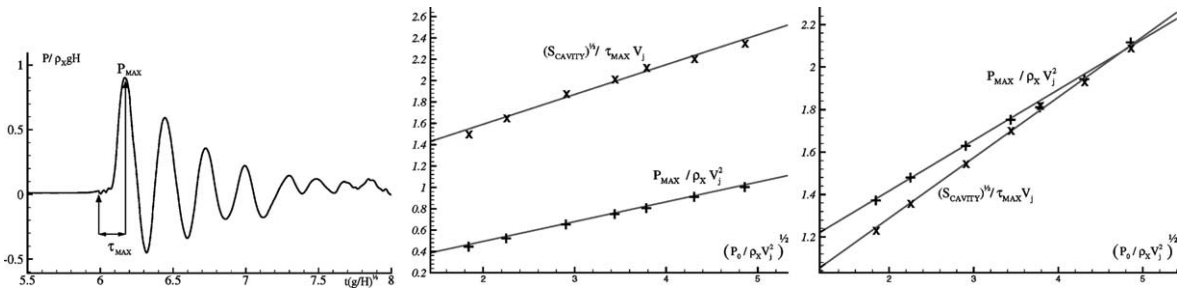


Fig. 23. Pressure oscillations inside the air bubble entrapped by the backward plunging breaker. Same case as in Fig. 3 with  $P_{0,Y}/\rho_X gH = 4.11, 6.15, 10.2, 14.3, 17.4, 22.5, 28.6$ . Left: time history of the bubble pressure oscillations for  $P_{0,Y}/\rho_X gH = 17.4$ . Center: effect of compressibility on peak and rise time of the bubble pressure. Right: effect of compressibility on peak and rise time of the wall pressure.

Finally, during the early stage of violent impact phenomenon, shock waves may be generated. In this circumstances a more general state equation for the gas should be used, for example of the type  $p = p(e, \rho)$ . This requires the solution of the Euler equations, including the equation for the internal energy  $e$ . Though gas-dynamic problems have been successfully solved by SPH, we have never attempted to couple the weakly compressible scheme for the water phase with a more general treatment of the air dynamics.

#### 4. Conclusions

An implementation of the SPH method to deal with two-dimensional interface flows with low density-ratios has been presented. The method results stable and capable to easily treat a variety of air–water flows with interface breaking and air-entrapment. In particular, the proposed form of the interactions terms is the basic tool to keep the algorithm stable for small density ratios. Second, a density re-initialization procedure is introduced which improves the mass-area-density consistency [3] and filters out small-scale pressure oscillations. This is also beneficial with respect to energy conservation when artificial viscosity is simultaneously used. Finally, a modified form of the artificial viscosity is proposed which improves the quality of the results through a more selective action.

An extended verification of the method has been presented through comparison with results obtained by the boundary-element method in the pre-breaking regime, and by the Level-Set technique for the Navier–Stokes equations further in the post-breaking regime. The agreement is rather good, and the differences fall in the uncertainty typical of each method.

The method is applied to study in more details the prototype two-dimensional flow arising after the break of a dam, with the water front impacting against a vertical wall placed at some distance from the broken dam and eventually forming a backward plunging breaker entrapping air. Comparisons with other numerical solvers, shallow-water theory and experiments have been presented to give a robust verification of the method prior the impact occurs. The effect of the density ratio on the global features of the studied phenomenon is discussed.

Finally, air-entrapment effects on the impact loads have been analyzed for the air–water case. It is shown that the free-surface flow modelling develops unphysical results, while the present two-phase model method captures qualitatively the evolution observed in some experimental results, although the quantitative agreement with the latter is not always satisfactory. As discussed in the referred experimental literature, pressure measurements during violent wave–structure interactions are highly scattered and many phenomena may hamper the comparison with the present two-dimensional computations. An analysis based on Bagnold theory of the pressure peak inside the air cavity and on the vertical wall seems to better confirm the reliability of the present results. Probably, an experimental activity based on force measurements could be more suitable for the validation of the present modelling and for further physical insights.

Modelling longer time evolutions of such phenomena would require the solution of the Navier–Stokes equations, because of the viscous dynamics of the generated rotational structures, and to account for surface-tension effects, in case of small geometrical scales. On the other side, for practical purposes, larger interest is on (short-time) impact loads and, from this perspective, a more important step is the extension of the method to the three-dimensional case, which is presently undertaken.

#### Acknowledgements

This work has been partly supported as part of a program for the simulation of ship breaking waves by the Ship Hydrodynamics Program of ONR, managed by Dr. Pat Purtell. INSEAN research activity was

supported by the Italian *Ministero delle Infrastrutture e Trasporti* through INSEAN Research Program 2000-02.

## References

- [1] R.A. Bagnold, Interim report on wave pressure research, J. Inst. Civil Eng. June (1939) 202–226.
- [2] T. Belytschko, Y. Krongauz, J. Dolbow, C. Gerlach, On the completeness of meshfree particle methods, Int. J. Numer. Mech. Eng. 43 (1999) 785–819.
- [3] W. Benz, Smooth particle hydrodynamics: a review, in: J.R. Buchler (Ed.), The Numerical Modelling of Nonlinear Stellar Pulsation, Kluwer Academic Publishers, Dordrecht, 1990, pp. 269–288.
- [4] G.V. Bicknell, The equation of motion of particles in smoothed particle hydrodynamics, SIAM J. Sci. Statist. Comput. 12 (1991) 1198–1206.
- [5] J. Bonet, T.-S.L. Lok, Variational and momentum preservation aspects of SPH formulations, Comput. Methods Appl. Mech. Eng. 180 (1999) 97–115.
- [6] A. Colagrossi, M. Landrini, M.P. Tulin, A Lagrangian meshless method for free-surface flows, in: Proc. 4th Numerical Towing Tank Symposium, Hamburg, 2001.
- [7] G. Colicchio, A. Colagrossi, M. Greco, M. Landrini, Free-surface flow after a dam break: a comparative study, Ship Tech. Res. 49/3 (2002).
- [8] G. Colicchio, M. Landrini, J.C. Chaplin, Level-set modelling of the air–water flow generated by a surface piercing body, in: Proc. 8th Int. Conf. on Numerical Ship Hydrodynamics, Korea, 2003.
- [9] E. Cumberbatch, The impact of a water wedge on a wall, J. Fluid Mech. 7 (1960) 353–374.
- [10] S.J. Cummins, M. Rudman, An SPH projection method, J. Comput. Phys. 152 (1999) 584–607.
- [11] O.M. Faltinsen, M. Landrini, M. Greco, Slamming in marine applications, J. Eng. Math. (2003), to be published.
- [12] M. Greco, M. Landrini, O.M. Faltinsen, Impact flows and loads on ship-deck structures, J. Fluids Struct. (2003), submitted.
- [13] W.G. Hoover, Isomorphism linking smooth particles and embedded atoms, Physica A 260 (1998) 244–254.
- [14] S. Koshizuka, Y. Oka, Moving-particle semi-implicit method for fragmentation of incompressible fluid, Nuclear Sci. Eng. 123 (1996) 421–434.
- [15] M. Landrini, A. Colagrossi, M.P. Tulin, Breaking bow and stern waves: numerical simulations, in: Proc. 16th Int. Work. Water Waves Float. Bodies, Hiroshima, Japan, 2001a.
- [16] M. Landrini, A. Colagrossi, M.P. Tulin, Numerical studies of breaking bow waves compared to experimental observations, in: Proc. 4th Numerical Towing Tank Symposium, Hamburg, Germany, 2001b.
- [17] N. Lanson, J.P. Vila, Meshless methods for conservation laws, Math. Comput. Simulation 55 (2001) 493–501.
- [18] J.C. Martin, W.J. Moyce, An experimental study of the collapse of liquid columns on a rigid horizontal plane, Philos. Trans. Roy. Soc. London, Ser. A 244 (1952) 312–324.
- [19] J.J. Monaghan, An introduction to SPH, Comput. Phys. Commun. 48 (1988) 89–96.
- [20] J.J. Monaghan, Smoothed particle hydrodynamics, Ann. Rev. Astronom. Astrophys. 30 (1992) 543–574.
- [21] J.J. Monaghan, Simulating free surface flows with SPH, J. Comput. Phys. 110 (1994) 399–406.
- [22] J.J. Monaghan, R.A. Gingold, Shock simulation by the particle method SPH, J. Comput. Phys. 52 (1983) 374–389.
- [23] J.J. Monaghan, A. Kocharyan, SPH simulation of multi-phase flow, Comput. Phys. Commun. 87 (1995) 225–235.
- [24] J.J. Monaghan, R.A.F. Cas, A.M. Kos, M. Hallworth, Gravity currents descending a ramp in a stratified tank, J. Fluid Mech. 379 (1999) 39–69.
- [25] J.J. Monaghan, A. Kos, Solitary Waves on a cretan beach, J. Waterway, Port, Coastal, Ocean Eng. May/June (1999) 145–154.
- [26] J.P. Morris, Analysis of smoothed particle hydrodynamics with applications, Ph.D. Dissertation Thesis, Dept. Math. Monash Un., 1996.
- [27] J.P. Morris, P.J. Fox, Y. Zhu, Modeling low reynolds number incompressible flows using SPH, J. Comput. Phys. 136 (1997) 214–226.
- [28] J.P. Morris, Simulating surface tension with smoothed particle hydrodynamics, Int. J. Numer. Methods Fluids 33 (2000) 333–353.
- [29] S. Nugent, H.A. Posch, Liquid drops and surface tension with smoothed particle applied mechanics, Phys. Rev. E 62 (4) (2000) 4968–4975, Part A.
- [30] H. Peregrine, L. Thais, The effect of entrained air in violent water wave impacts, J. Fluid Mech. 325 (1996) 337–397.
- [31] H. Peregrine, Water-wave impact on walls, Ann. Rev. Fluid Mech. 35 (2003) 23–43.
- [32] F.V. Pohle, The Lagrangian Equations of Hydrodynamics: Solutions Which are Analytic Functions of the Time, Grad. School of Arts and Science of New York Univ., New York, 1950.
- [33] A. Ritter, Die fortpflanzung der wasserwellen, Z. Ver. deut. Ing. 36 (1982).

- [34] R. Scardovelli, S. Zaleski, Direct numerical simulation of free-surface and interfacial flow calculations, *Ann. Rev. Fluid Mech.* 31 (1999) 567–603.
- [35] J.A. Sethian, P. Smereka, Level-set methods for fluid interfaces, *Ann. Rev. Fluid Mech.* 35 (2003) 341–372.
- [36] P.K. Stansby, A. Chegini, T.C.D. Barnes, The initial stages of dam-break flow, *J. Fluid Mech.* 374 (1998) 407–424.
- [37] M. Sussman, P. Smereka, S. Osher, A level set approach for computing solutions to incompressible two-phase flow, *J. Comput. Phys.* 114 (1994) 146–159.
- [38] J.W. Swegle, D.L. Hicks, S.W. Attaway, Smoothed particle hydrodynamics stability analysis, *J. Comput. Phys.* 116 (1995) 123–134.
- [39] S. Zhang, D.K.P. Yue, K. Tanizawa, Simulation of plunging wave impact on a vertical wall, *J. Fluid Mech.* 327 (1996) 221–254.
- [40] Z.Q. Zhou, J.O. De Kat, B. Buchner, A nonlinear 3-D approach to simulate green water dynamics on deck, in: J. Piquet (Ed.), *Proc. 7th Int. Conf. Num. Ship Hydrod.*, Nantes, 1999, pp. 5.1–1, 15.